Quantum spin Hall effect from multiscale band inversion in twisted bilayer $Bi_2(Te_{1-x}Se_x)_3$

Ikuma Tateishi [1,*] and Motoaki Hirayama [1,2,3,†]

[1] *RIKEN Center for Emergent Matter Science, Wako, Saitama 351-0198, Japan*
[2] *Department of Applied Physics, University of Tokyo, Tokyo 113-8656, Japan*
[3] *JST, PRESTO, Hongo, Bunkyo-ku, Tokyo 113-8656, Japan*

(Received 7 March 2022; revised 3 August 2022; accepted 8 September 2022; published 18 October 2022)

Moiré materials have become one of the most active fields in material science in recent years due to their high tunability, and their unique properties emerge from the moiré-scale structure modulation. Here, we propose twisted bilayer $Bi_2(Te_{1-x}Se_x)_3$ as a moiré material where the moiré-scale modulation induces a topological phase transition. We show, in twisted bilayer $Bi_2(Te_{1-x}Se_x)_3$, a topological insulator domain and a normal insulator domain coexist in the moiré lattice structure, and edge states on the domain boundary make nearly flat bands that dominate the material properties. The edge states further contribute to a moiré-scale band inversion, resulting in moiré-scale topological states. There are corresponding moiré-scale edge states and they are so to speak "edge state from edge state," which is a unique feature of twisted bilayer $Bi_2(Te_{1-x}Se_x)_3$. Our result not only proposes characteristic quantum phases in twisted bilayer Bi_2Te_3 family, but also suggests the twisting of stacking-sensitive topological materials paves an avenue in the search for novel quantum materials and devices.

DOI: 10.1103/PhysRevResearch.4.043045

I. INTRODUCTION

The twisted van der Waals heterostructure materials, or moiré materials, have been studied very intensively in recent years as a platform for exploring novel quantum phases [1–24]. In those materials, moiré superlattices are formed by the lattice misalignment with a small twist angle, and the moiré superlattices produce flat electric bands and various strongly correlated phases. In particular, the experimental reports on the magic-angle twisted bilayer graphene have stimulated this field [1,2]. They reported that the bilayer graphene stacked with a twist angle 1.08° (magic angle), which has been known to have flat bands near the Fermi level, shows correlated insulating phases and superconducting phases when the filling factor is tuned. Because the behavior resembles the phase diagram of the high-temperature cuprate superconductors, twisted bilayer graphene has attracted great attention. The unique feature of the moiré material is its high tunability. The twist angle is a tunable parameter specific to moiré materials. Furthermore, because the system is two-dimensional (2D) and has a large moiré unit cell, the filling factor can be tuned easily and significantly. This high tunability allows us to find various quantum phases in a single moiré material. Inspired by the twisted bilayer graphene, moiré systems of some other layered materials have been studied. In the twisted bilayer transition metal dichalcogenides (TMD), nearly flat bands have been theoretically predicted on the valence band edge, and an experimental signature of a correlated insulator phase has been reported [25–36]. Also for other materials, such as hexagonal boron nitride (hBN), the existence of nearly flat bands has been suggested [37,38]. Although the tunability of moiré materials is remarkable, research of moiré materials has concentrated on the layered materials above. Hence, the physics that describes their low-energy electronic states can be qualitatively categorized into two groups, semimetallic one (graphene) and insulating ones (TMD, hBN).

In this paper, we theoretically propose twisted bilayer $Bi_2(Te_{1-x}Se_x)_3$ (Fig. 1) as a moiré material that hosts characteristic low-energy electronic states described by a topological phase transition and corresponding topological edge states. Three-dimensional bulk $Bi_2(Te_{1-x}Se_x)_3$ is one of the van der Waals heterostructure materials, and is well known as a typical strong topological insulator [39–42]. For the thin-film $Bi_2(Te_{1-x}Se_x)_3$ case, it has been suggested that the topological invariant strongly depends on the number of stacked layers [43]. Therefore, topological phase transitions are expected to occur when the stacking order or interlayer distance is changed. Generally in a moiré material, the local stacking order and interlayer distance are modulated by the lattice misalignment [20]. Combining the stacking modulation and the stacking-sensitive topological insulator, we propose a Moiré material with mixed topological insulator domain and normal insulator domain.

II. EFFECTIVE MODEL FOR MOIRÉ MATERIALS

In this paper, to avoid confusion, an atomic-scale lattice structure in an untwisted system is explicitly referred to

*ikuma.tateishi@riken.jp
†hirayama@ap.t.u-tokyo.ac.jp

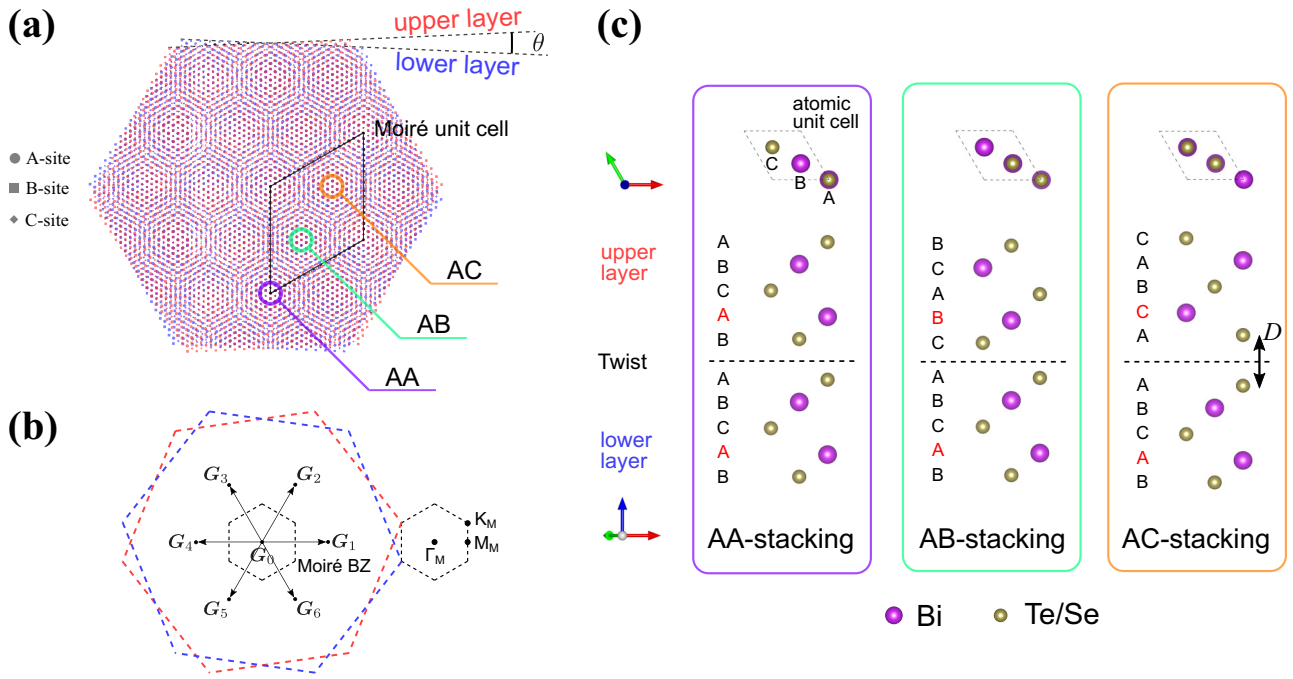

FIG. 1. Lattice structure of twisted bilayer $Bi_2(Te_{1-x}Se_x)_3$. (a) Schematic picture of the moiré pattern in twisted bilayer $Bi_2(Te_{1-x}Se_x)_3$. There are three in-plane atomic sites, A, B, and C sites, in the untwisted $Bi_2(Te_{1-x}Se_x)_3$. The atomic lattices in the upper and lower layers are drawn with red and blue markers, respectively. The solid rhombus represents the moiré unit cell. The three sampling points used in the effective model are denoted with circles. (b) Schematic picture of the moiré BZ. The red and blue dashed hexagons are twisted atomic BZ of the upper and lower layers, respectively. $\boldsymbol{G}_0 \sim \boldsymbol{G}_6$ are the moiré reciprocal lattice vectors that we used in the effective model. (c) Top and horizontal views of the atomic lattice structures of untwisted bilayer $Bi_2(Te_{1-x}Se_x)_3$ for AA (left), AB (middle), and AC stacking (right), drawn by VESTA [46]. Each of the upper and lower layers has five atoms in the atomic unit cell.

as "*atomic lattice*" and a moiré superlattice structure in a twisted system is referred as "*moiré lattice*" (Fig. 1). The words "atomic" and "moiré" are used in the same way for other terms, such as atomic (moiré) Brillouin zone (BZ). In $Bi_2(Te_{1-x}Se_x)_3$, the relation between an atomic lattice constant a and a moiré lattice constant L is written as $a = 2L \sin\frac{\theta}{2}$, where θ is a twist angle.

The moiré electronic states are calculated with an effective model within a small-angle approximation [44,45]. The Hamiltonian of the effective model is given as

$$H = \int d\boldsymbol{k} \sum_{\alpha\sigma,\beta'\sigma'} \sum_{\boldsymbol{G}_l} t^{\alpha\sigma,\beta'\sigma'}_{\boldsymbol{k},\boldsymbol{k}-\boldsymbol{G}_l,\boldsymbol{G}_l} c^{\dagger}_{\alpha\sigma,\boldsymbol{k}} c_{\beta'\sigma',\boldsymbol{k}-\boldsymbol{G}_l}, \tag{1}$$

where $\alpha\sigma$ and $\beta'\sigma'$ are orbital-spin indices, and $c^{\dagger}$ (c) is a creation (annihilation) operator. The sum $\sum_{\boldsymbol{G}_l}$ is taken over seven moiré reciprocal lattice vectors $\boldsymbol{G}_0 \sim \boldsymbol{G}_6$ ($\boldsymbol{G}_0 = \boldsymbol{0}$, $|\boldsymbol{G}_{l\neq 0}| = \frac{4\pi}{\sqrt{3}L}$) [Fig. 1(b)] as an approximation. The $t^{\alpha\sigma,\beta'\sigma'}_{\boldsymbol{k},\boldsymbol{k}-\boldsymbol{G}_l,\boldsymbol{G}_l}$ are determined to satisfy

$$\sum_{\boldsymbol{G}_l} e^{i\boldsymbol{G}_l\cdot\boldsymbol{r}_j} t^{\alpha\sigma,\beta'\sigma'}_{\boldsymbol{k},\boldsymbol{k}-\boldsymbol{G}_m,\boldsymbol{G}_l} = h^{\alpha\sigma,\beta'\sigma'}_{\boldsymbol{r}_j}(\boldsymbol{k}-\boldsymbol{G}_m/2), \tag{2}$$

where $h^{\alpha\sigma,\beta'\sigma'}_{\boldsymbol{r}_j}(\boldsymbol{k})$ are the matrix elements calculated from hopping parameters around position $\boldsymbol{r}_j$ (see Appendixes A, B, and C for more detail of the model derivation). The local atomic lattice structure around $\boldsymbol{r}_j$ is approximated by an untwisted lattice with a particular stacking order, and thus $h^{\alpha\sigma,\beta'\sigma'}_{\boldsymbol{r}_j}(\boldsymbol{k})$ and the electronic states on it are also estimated by calculation in the untwisted lattice. We take three sampling points of $\boldsymbol{r}_j$, and interpolate the intermediate region by the discrete Fourier transform. We call the three stacking orders at the three sampling points AA, AB, and AC stacking [Figs. 1(a) and 1(c)]. The AB stacking is the most stable one and thus it is realized in the three-dimensional (3D) bulk $Bi_2(Te_{1-x}Se_x)_3$. With the three sampling points approximation, the explicit definitions of $t^{\alpha\sigma,\beta'\sigma'}_{\boldsymbol{k},\boldsymbol{k}-\boldsymbol{G}_l,\boldsymbol{G}_l}$ are given as

$$\begin{aligned}
t^{\alpha\sigma,\beta'\sigma'}_{\boldsymbol{k},\boldsymbol{k},\boldsymbol{G}_0} &= \frac{1}{3}\left[h^{\alpha\sigma,\beta'\sigma'}_{\boldsymbol{r}_{AA}}(\boldsymbol{k}) + h^{\alpha\sigma,\beta'\sigma'}_{\boldsymbol{r}_{AB}}(\boldsymbol{k}) + h^{\alpha\sigma,\beta'\sigma'}_{\boldsymbol{r}_{AC}}(\boldsymbol{k})\right], \\
t^{\alpha\sigma,\beta'\sigma'}_{\boldsymbol{k},\boldsymbol{k}-\boldsymbol{G}_l,\boldsymbol{G}_l} &= \frac{1}{9}\left[h^{\alpha\sigma,\beta'\sigma'}_{\boldsymbol{r}_{AA}}(\boldsymbol{k}-\boldsymbol{G}_l/2) + e^{-i\frac{2\pi}{3}} h^{\alpha\sigma,\beta'\sigma'}_{\boldsymbol{r}_{AB}}(\boldsymbol{k}-\boldsymbol{G}_l/2)\right. \\
&\quad \left. + e^{i\frac{2\pi}{3}} h^{\alpha\sigma,\beta'\sigma'}_{\boldsymbol{r}_{AC}}(\boldsymbol{k}-\boldsymbol{G}_l/2)\right] \quad (l = 1,3,5), \\
t^{\alpha\sigma,\beta'\sigma'}_{\boldsymbol{k},\boldsymbol{k}-\boldsymbol{G}_l,\boldsymbol{G}_l} &= \frac{1}{9}\left[h^{\alpha\sigma,\beta'\sigma'}_{\boldsymbol{r}_{AA}}(\boldsymbol{k}-\boldsymbol{G}_l/2) + e^{i\frac{2\pi}{3}} h^{\alpha\sigma,\beta'\sigma'}_{\boldsymbol{r}_{AB}}(\boldsymbol{k}-\boldsymbol{G}_l/2)\right. \\
&\quad \left. + e^{-i\frac{2\pi}{3}} h^{\alpha\sigma,\beta'\sigma'}_{\boldsymbol{r}_{AC}}(\boldsymbol{k}-\boldsymbol{G}_l/2)\right] \quad (l = 2,4,6).
\end{aligned} \tag{3}$$

$h^{\alpha\sigma,\beta'\sigma'}_{\boldsymbol{r}_{AA}}(\boldsymbol{k})$, $h^{\alpha\sigma,\beta'\sigma'}_{\boldsymbol{r}_{AB}}(\boldsymbol{k})$, and $h^{\alpha\sigma,\beta'\sigma'}_{\boldsymbol{r}_{AC}}(\boldsymbol{k})$ are matrix elements of Hamiltonians calculated in the AA-, AB-, and AC-stacking untwisted bilayer $Bi_2(Te_{1-x}Se_x)_3$, respectively.

$h^{\alpha\sigma,\beta'\sigma'}_{\boldsymbol{r}_{AA}}(\boldsymbol{k})$, $h^{\alpha\sigma,\beta'\sigma'}_{\boldsymbol{r}_{AB}}(\boldsymbol{k})$, and $h^{\alpha\sigma,\beta'\sigma'}_{\boldsymbol{r}_{AC}}(\boldsymbol{k})$ are obtained by the first-principles calculation. All first-principles calculations are implemented in the Vienna *ab initio* simulation package (VASP) [47]. We use the projector augmented wave (PAW) potential sets recommended by VASP and set the kinetic-energy cutoff to 500 eV. For each of the three stacking orders, we

TABLE I. Optimized in-plane lattice constant a and interlayer distance D for bilayer Bi_2Te_3 and Bi_2Se_3 with three stacking orders. The AA, AB, and AC stackings are defined in Fig. 1.

Bi_2Te_3	AA	AB	AC
In-plane lat. const. a (Å)	4.40	4.41	4.39
Interlayer distance D (Å)	3.18	2.73	3.98
Bi_2Se_3	AA	AB	AC
In-plane lat. const. a (Å)	4.15	4.16	4.15
Interlayer distance D (Å)	3.05	2.75	3.78

optimize the lattice structure and obtain electronic band structures. The lattice optimizations are performed in the strongly constrained and appropriately normed (SCAN) metageneralized gradient approximation for short- and intermediate-range interactions with the long-range van der Waals (vdW) interaction (rVV10) with the spin-orbit interaction [48]. We calculate the electronic band structure in the B3LYP with the VWN3 correlation [49]. We construct Wannier functions for the Bi and Te/Se p orbitals with WANNIER90 package [50]. We use $8 \times 8 \times 1$ k mesh for the lattice optimization and $9 \times 9 \times 1$ k mesh for the electronic calculation and the Wannier function. The obtained band structures reproduce well the results of angle-resolved photoemission spectroscopy (ARPES) [51,52] and the GW approximation [53]. The Fermi level is set in the averaged Hamiltonian of three stacking orders $t^{\alpha\sigma,\beta'\sigma'}_{\boldsymbol{k},\boldsymbol{k},\boldsymbol{G}_0}$ by the filling factor, i.e., the middle of the 36th and 37th bands in the Γ point of the 60 bands (2 layers $\times 5$ atoms $\times p$ orbitals $\times$ spin). The obtained Wannier functions and matrix elements are also used in the calculations of the Wilson loop spectra with the WANNIERTOOLSpackage [54]. We also calculate the Sb_2Te_3 under the same condition (see Appendix D).

III. BILAYER $Bi_2(Te_{1-x}Se_x)_3$

First, we show the result of calculations on the untwisted atomic lattices of bilayer Bi_2Te_3 and Bi_2Se_3 for the three stacking orders. The atomic positions are shown in Fig. 1(c). All these untwisted bilayer lattices belong to the layer group No. 72 (or the space group No. 166 with infinitely long c axis). The optimized in-plane lattice constant a and interlayer distance D, which is defined as the vertical distance between the two Te/Se atoms in the twist face [see Fig. 1(c), right], are listed in Table I. We neglect the stacking order dependence in the in-plane lattice constant in each material and use an averaged value in the effective model calculations. For Te/Se doping, the in-plane lattice constant is linearly interpolated. In both materials, the AB stacking has the smallest interlayer distance and the AC stacking has the largest. The obtained electronic band structures are shown in Figs. 2(a)–2(f) for both of Bi_2Te_3 and Bi_2Se_3, where the Fermi level is determined by the filling factor. The magenta and yellow dots represent the projected weight on the p_z orbitals of Bi and (Te,Se) atoms, respectively. In these materials, the overlap of the p_z orbitals contributes to a topological phase transition. Therefore, the smaller the interlayer distance, the more likely it is to be a topological insulator. To evaluate their topological invariants, we make Wannier functions for them and calculate the Wilson loop spectra as shown in the right panel of each figure of Figs. 2(a)–2(f). We can see only AB-stacking Bi_2Te_3 is a topological insulator and all of the others are normal insulators. These results indicate that a twisted bilayer Bi_2Te_3 system has a topological insulator domain around the AB-stacking

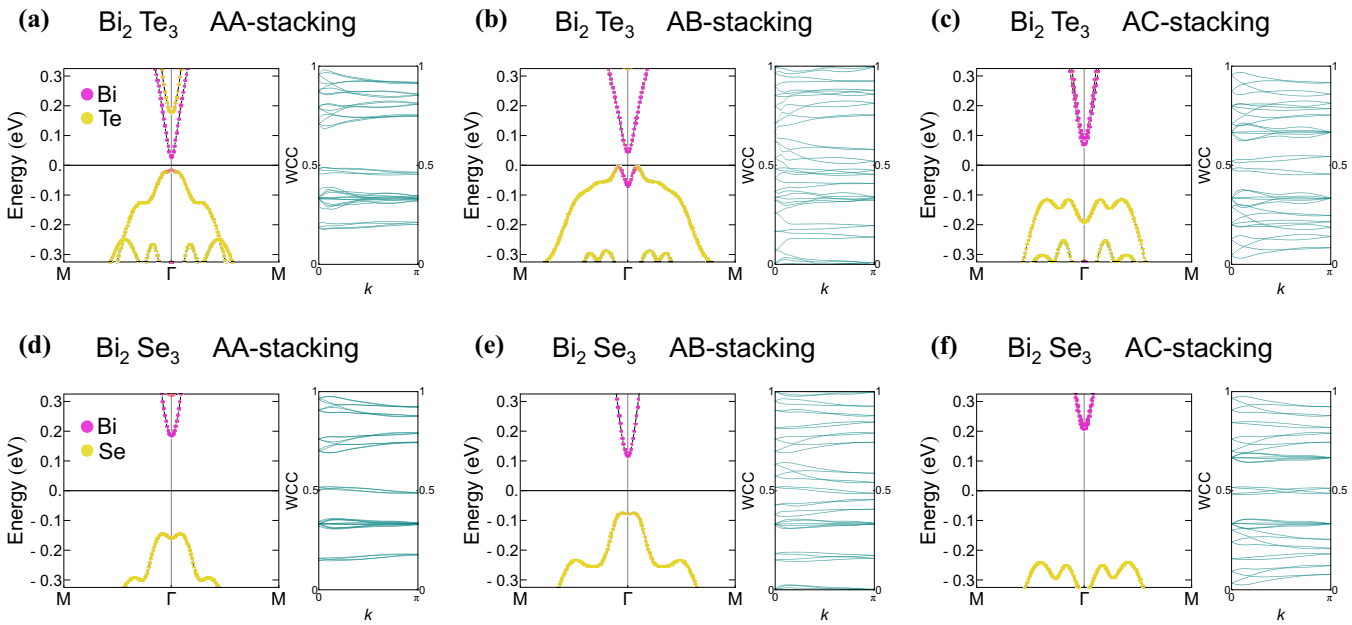

FIG. 2. Electronic band structure and Wilson loop spectra of the untwisted bilayer Bi_2Te_3 and Bi_2Se_3 for each stacking order. (a)–(c) For AA-, AB-, and AC-stacking bilayer Bi_2Te_3, and (d)–(f) are for those of bilayer Bi_2Se_3, respectively. The magenta and yellow dots in the band structure figures represent the projected weight on the p_z orbitals of Bi and Te/Se atoms, respectively. Only AB-stacking bilayer Bi_2Te_3 (b) is a topological insulator, and the others are normal insulators.

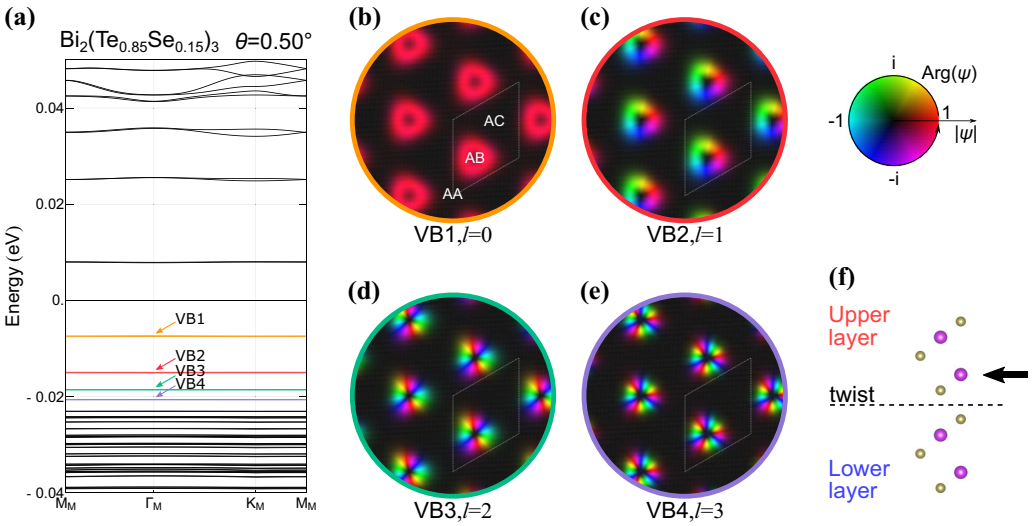

FIG. 3. Moiré band structure of twisted bilayer $Bi_2(Te_{1-x}Se_x)_3$. (a) Moiré band dispersion of $Bi_2(Te_{0.85}Se_{0.15})_3$ with a twist angle $\theta = 0.50°$. The top (VB1), second (VB2), third (VB3), and fourth (VB4) valence band pairs are shown as orange, red, green, and purple lines, respectively. The symbols of the high-symmetry points are defined in Fig. 1(b). (b)–(e) Real-space plot of the wave functions [upper layer, lower Bi, p_z orbital, spin-up component, as shown in (f)] of VB1-4 in the Γ_M point. The brightness and color indicate the absolute value (normalized to have the maximum value of 1) and phase of the wave function as shown in the right of (c). The moiré unit cell is shown as a white dashed rhombus. The angular momentum l is also shown in each figure. (f) Bi atom that is focused in the plots.

region, and a normal insulator domain in the other region. Although Bi_2Se_3 is a normal insulator in the three stacking orders, we consider Se doping in Bi_2Te_3 by the linear interpolation to tune the system parameters. However, note that the topological nontriviality of the AB-stacking Bi_2Te_3 plays an essential role even in doped cases.

IV. MOIRÉ BAND AND QUANTIZED EDGE STATE IN TWISTED BILAYER $Bi_2(Te_{1-x}Se_x)_3$

Next, we show the moiré band dispersion of twisted bilayer $Bi_2(Te_{1-x}Se_x)_3$. Due to the twisting, the inversion symmetry is broken and twisted bilayer $Bi_2(Te_{1-x}Se_x)_3$ belongs to the layer group No. 67 (or the space group No. 149 with infinitely long c axis). The in-plane C_2 axis exists along the (AA-AB-AC)-stacking line [see Fig. 1(a)], which corresponds to the Γ_M-M_M line in the reciprocal space. The symbols of the high-symmetry points in the moiré BZ are defined as Fig. 1(b). Figure 3(a) shows the band dispersion of the twisted bilayer $Bi_2(Te_{0.85}Se_{0.15})_3$ with a twist angle $\theta = 0.50°$. Here, to obtain a clear domain boundary, the amount of Se (x) is determined so that the gap in the AA and AB stacking would be roughly the same (see Appendix D for the detail of Se-doping dependence of the gap and moiré band dispersion). All bands are doubly degenerate at time-reversal invariant momenta (TRIM), the Γ_M and M_M points. Because of the absence of the inversion symmetry, the Kramers degeneracy in the untwisted bilayer splits at a general momentum. The split is easy to see in the conduction bands above 0.020 eV in the K_M point, while it is too small to see in the valence bands. It is worth noting that there are nearly flat bands around the Fermi level. For the nearly flat valence bands [from the top to fourth valence band pairs VB1, VB2, VB3, and VB4 in Fig. 3(a)], real-space plots of the wave functions (upper layer, lower Bi, p_z orbital, spin-up component; see Fig. 3(f)] at the Γ_M point are shown in Figs. 3(b)–3(e). The brightness and color indicate the absolute value (normalized to have the maximum value of 1) and phase of the wave function, respectively [as shown in the right of Fig. 3(c)]. The wave function has a ring-shaped density distribution, clearly indicating that these nearly flat bands originate from the edge state corresponding to the topological insulator domain around the AB-stacking area. To compare with the wave functions of the flat bands, we calculate the real-space dependence of the band gap between the valence top and conduction bottom bands in the Γ point $\Delta E(\Gamma)$ in the interpolated untwisted Hamiltonian obtained by the discrete Fourier transform in Eq. (2) (see Appendix D for more detail). In Fig. 4, the real-space dependence of the band bap (violet line) and the absolute value of the wave function of VB2 (cyan line) along the (AA-AB-AC-AA)-stacking line (the longer diagonal of the moiré unit cell shown as a white arrow) are shown. The negative band gap means that the bands are inverted. The gapless points are the domain boundary and the topological insulator domain is shown as a green-shaded range. We can confirm that the wave function has a large amplitude around the domain boundary. Next, we focus on the difference between the wave functions of VB1-4 [Figs. 3(b)–3(e)]. They show ring-shaped density distributions in common, but their phase structures are different from each other. We can see a lower energy band has a larger angular momentum l, which is calculated as a winding number of the phase along the ring. Note that because these states are coupled with spin, the spin-down component has one different l and the total angular momentum is a half-integer (see Appendix E for more detail). The phase structure indicates that the nearly flat bands are formed by quantization of topological edge states due to the finite-size effect of the domain boundary. The flatness of these bands and the gap size between them depend on the twist angle. Figures 5(a)–5(c) show the twist angle dependence of

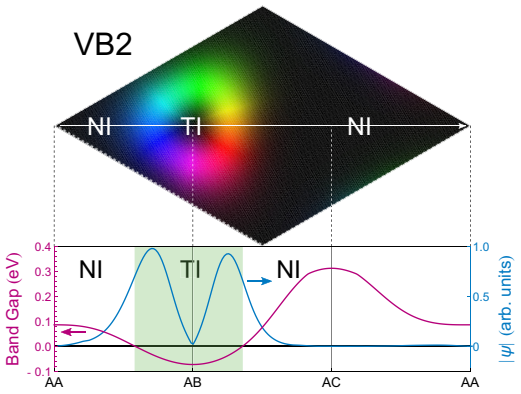

FIG. 4. Moiré wave function and local electronic state. The rhombus is a wave-function plot of VB2 in the moiré unit cell [same as Fig. 3(c)]. The lower plot shows the real-space dependence of the absolute value of the wave function of VB2 (cyan line, right vertical axis) and the band gap calculated in the interpolated untwisted Hamiltonian (violet line, left vertical axis). The horizontal axis is the real-space position along the (AA-AB-AC-AA)-stacking line, which is the longer diagonal of the moiré unit cell as shown with a white arrow in the top figure. The negative band gap means that the bands are inverted. The two gapless points around the AB-stacking area are the domain boundary, and the topological insulator domain is shown as a green-shaded range.

the moiré band dispersion. It can be seen that as the twist angle increases, the nearly flat bands get more dispersive and the energy gaps between them get larger. This twist angle dependence is explained by the angle dependence of the effect of moiré modulation terms [$t^{\alpha\sigma,\beta'\sigma'}_{\boldsymbol{k},\boldsymbol{k}-\boldsymbol{G}_l,\boldsymbol{G}_l}$, $l \neq 0$ in Eq. (3)], in which interlayer components play a major role. As in Eq. (1), the moiré modulation terms couple the atomic Bloch states at $\boldsymbol{k}$ and $\boldsymbol{k}+\boldsymbol{G}_l$. Hence, the effects of the moiré modulation terms are interpreted as a hybridization between moiré bands given by band folding with the moiré BZ. The twist angle dependence of them appears in $\boldsymbol{G}_l$ as $|\boldsymbol{G}_l| \propto \theta$, while the amplitude $|t^{\alpha\sigma,\beta'\sigma'}_{\boldsymbol{k},\boldsymbol{k}-\boldsymbol{G}_l,\boldsymbol{G}_l}|$ are independent of θ. For a smaller twist angle, the moiré modulation terms get relatively larger than the bandwidth of the folded moiré bands, and thus their effects, which make a gap and flatten the moiré bands, get more significant. A concrete picture for the $Bi_2(Te_{1-x}Se_x)_3$ case is illustrated in Fig. 5(d). The moiré bands around the Fermi level are basically formed by folding the original Dirac cone of the edge state on the domain boundary with the moiré BZ. In a smaller angle case, the original Dirac cone is folded into many smaller parts and the moiré modulation terms make more flat moiré bands with smaller gaps. This picture is consistent with the angular momentum sequence of the wave functions at the Γ point. The band-flattening effect of the moiré modulation terms and its twist angle dependence are also understood in a perspective of a spread of a the wave function and a coupling strength between edge states around the neighbor TI domains. For smaller twist angle, there are more moiré bands in the typical energy range of the moiré modulation. As a result, the moiré bands are made by hybridizing more states with shorter wavelengths, and less spread wave functions in the moiré unit cell can be obtained [Figs. 5(a)–5(c), bottom]. It means the coupling strength between edge states around the neighbor TI domains gets weaker for a smaller twist angle, and thus more flat moiré bands are obtained (see Appendix E for more detail). Note also that as the wave function spreads, the effect of the moíre unit-cell shape becomes significant and the anisotropy of the distribution of the wave function (triangular in this case) becomes more pronounced. With these

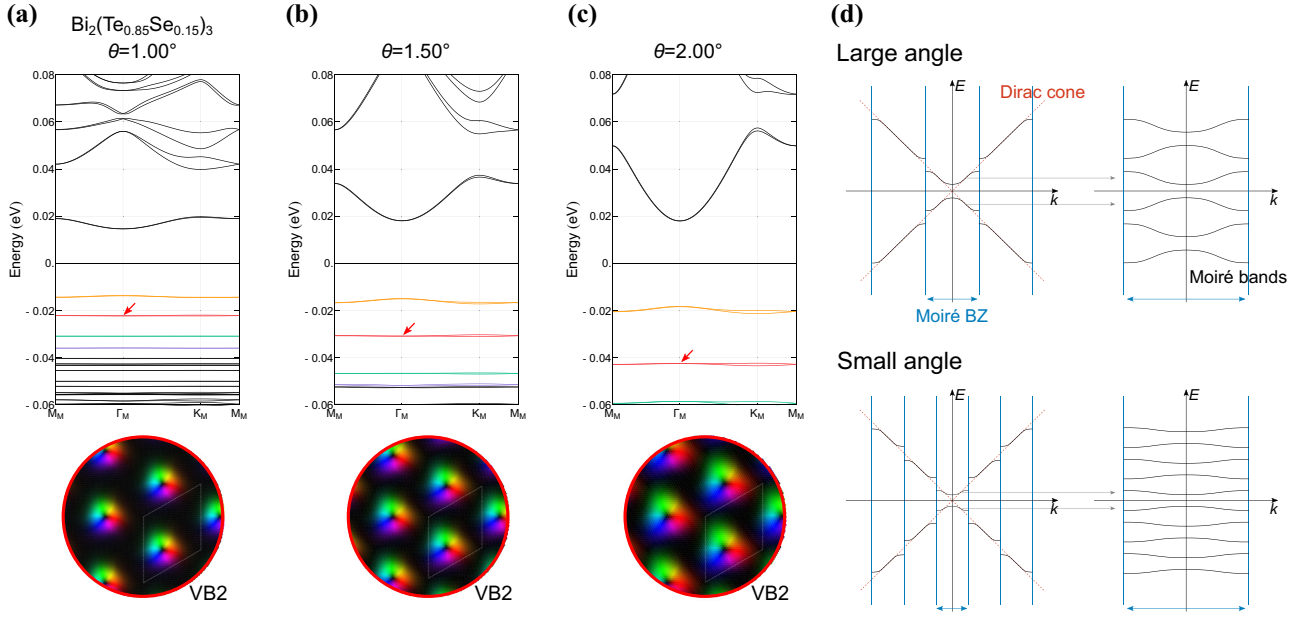

FIG. 5. Twist angle dependence of moiré band dispersion and wave functions of $Bi_2(Te_{0.85}Se_{0.15})_3$. (a)–(c) The cases with a twist angle $\theta = 1.00°$, 1.50°, and 2.00°, respectively. VB1-4 are shown with the same color as Fig. 3(a). The wave functions of the VB2 bands are plotted in the same way as Fig. 3. (d) Schematic picture to explain the twist angle dependence of the flatness and gap of the edge-state-originated nearly flat bands.

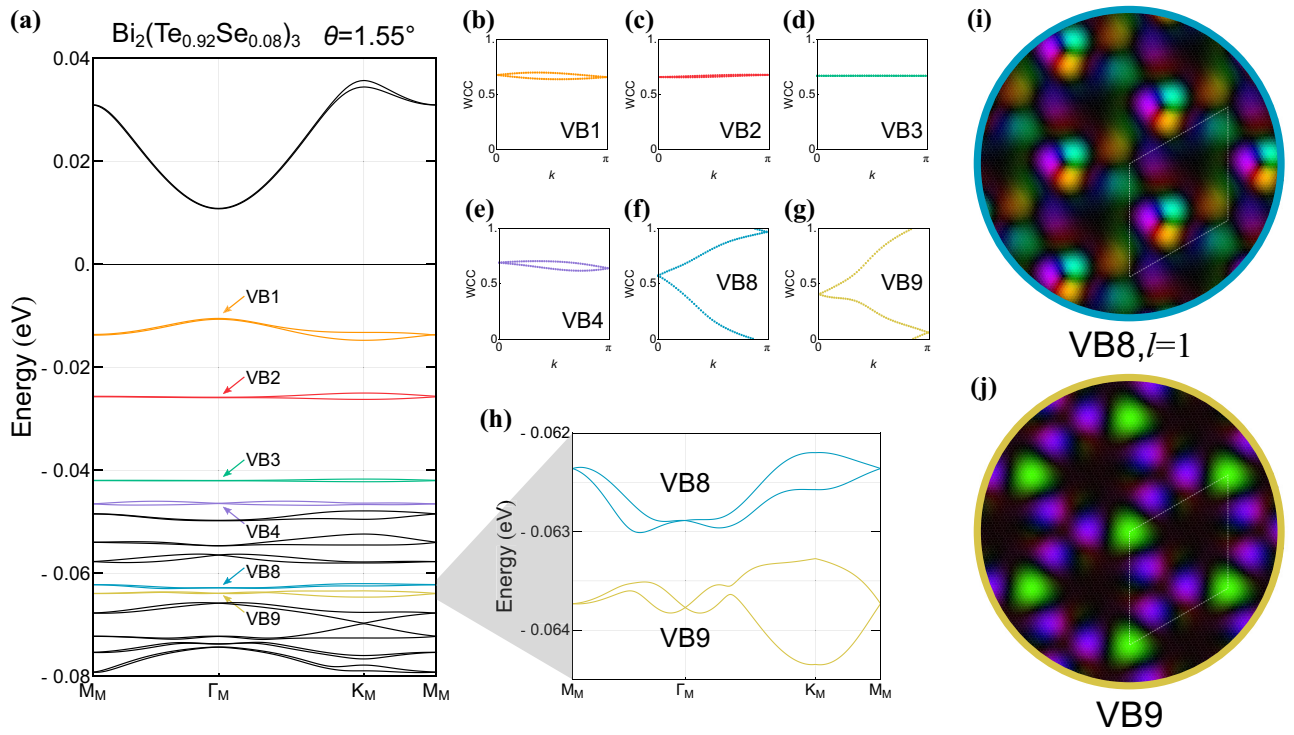

FIG. 6. Quantum spin Hall effect in twisted bilayer $Bi_2(Te_{1-x}Se_x)_3$. (a) Moiré band dispersion of $Bi_2(Te_{0.92}Se_{0.08})_3$ with a twist angle $\theta = 1.55^\circ$. The top (VB1), second (VB2), third (VB3), fourth (VB4), eighth (VB8), and ninth (VB9) valence band pairs are shown as orange, red, green, purple, blue, and yellow lines, respectively. (b)–(g) Wilson loop spectra calculated on VB1-4, VB8, and VB9. While (b)–(e) VB1-4 are topologically trivial, (f) VB8 and (g) VB9 are topologically nontrivial. (h) Magnified view of the VB8 and VB9. In this figure. the numerical error due to the first-principles calculation is corrected to recover the exact time-reversal symmetry. (i), (j) Real-space plot of the wave functions (upper layer, lower Bi, p_z orbital, spin-up component) of VB8 and VB9 in the Γ_M point, respectively. VB8 has a ring-shaped density distribution around the AB-stacking area, but VB9 has no longer ring-shaped one but localized density distribution around the AA-stacking area.

points of view, the twist angle dependence of the flatness and energy gap of the edge-state-originated nearly flat bands is roughly explained, but, in more detail, the effect of the Rashba splitting and hybridization with other bands must be taken into account.

Finally, we mention the conduction bands. In $Bi_2(Te_{1-x}Se_x)_3$ case, since the conduction bands are more dispersive than the valence bands in the band structures of untwisted lattices, the moiré conduction bands are also more likely to have dispersion in the higher-energy region. For the same reason, a band gap between moiré conduction bands tends to be larger than that of moiré valence bands.

V. MOIRÉ-SCALE TOPOLOGICAL BAND AND EDGE STATE

We move on to a discussion of the emergence of topological bands in the moiré bands of twisted bilayer $Bi_2(Te_{1-x}Se_x)_3$. As we discussed above, the formation of the edge-state-originated nearly flat bands is explained by a simple theory and they are ordered with angular momentum l. Therefore, we could not find a case to have a band inversion between the edge-state-originated bands. However, in the region farther from the Fermi level, a bulk-state-originated band appears and it can hybridize with an edge-state-originated to form topologically nontrivial bands. For example, the band dispersion of $Bi_2(Te_{0.92}Se_{0.08})_3$ with a twist angle $\theta = 1.55^\circ$ is shown in Fig. 6(a). Here, the amount of Se (x) is determined so that the gap in the AA-stacking area would be smaller than that of the AB-stacking area to obtain the bulk and edge states in different areas. To evaluate the topological invariants for each band, the Wilson loop spectra are calculated and given in Figs. 6(b)–6(g). While the nearly flat band around the Fermi level [VB1-4, Figs. 6(b)–6(e)] are evaluated as topologically trivial, the bands around -0.065 eV [the eighth and ninth valence band pairs VB8 and VB9, Figs. 6(f) and 6(g)] are evaluated as topologically nontrivial. Figure 6(h) is a magnified view of the VB8 and VB9. Here, we correct the numerical error due to the first-principles calculation to recover the exact time-reversal symmetry because the moiré system generally deals with a small energy scale and thus the numerical errors get more noticeable. It can be seen that the two bands are gapped and thus if the Fermi level is tuned and placed between them the system becomes a topological insulator protected by the time-reversal symmetry. The real-space plots of the wave functions in the Γ_M point of the two bands are shown in Figs. 6(i) and 6(j). The wave function of VB8 [Fig. 6(i)] has a ring-shaped density distribution as well as the nearly flat bands around the Fermi level. On the other hand, VB9 [Fig. 6(j)] does not have a ring-shaped one, but has a density distribution localized around the AA-stacking area (the corner of the moiré unit cell). Considering that the AA-stacking Bi_2Te_3 has the smallest gap among all stacking orders (Fig. 2), this state is understood as a state originated from the bulk state

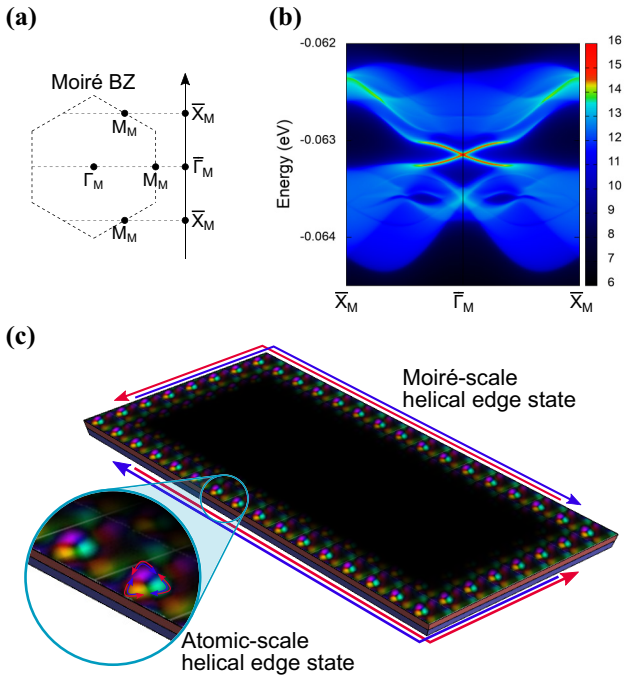

FIG. 7. Topological edge state in twisted bilayer $Bi_2(Te_{1-x}Se_x)_3$. (a) Moiré-scale edge BZ that is used in the edge calculation. (b) Edge band spectrum around VB8 and VB9. The symbols of the high-symmetry points are defined in (a). Dirac cones of the moiré-scale helical edge state can be seen appearing around the $\bar{\Gamma}_M$ point. (c) Schematic picture of "edge state from edge state." The red and blue arrows correspond to spin currents having opposite spin directions to each other. The helical edge state obtained in moiré bands (moiré-scale helical edge state) is running along the edge of the moiré-scale lattice system. The moiré-scale edge state is made from the ring-shaped edge state on the domain boundary around the AB-stacking area (atomic-scale helical edge state).

of the AA-stacking area. Due to a symmetry restriction of the hybridization, the simple bulk-state-originated band can hybridize with a band with a small l. That is why the VB8 has $l = 1$ (as we explained, the spin-down component has one different l). To obtain edge states corresponding to these topological bands, we make Wannier functions for these bands and calculate the edge band spectra with Green's function method (technical details are described in Appendix C). The moiré-scale edge BZ that is used in the edge calculation is shown in Fig. 7(a). The obtained edge band spectrum is shown in Fig. 7(b). As in a typical topological insulator, a Dirac cone of the helical edge state can be seen appearing around the $\bar{\Gamma}_M$ point (see Appendix E for a symmetry restriction on the Dirac cone). These topological bands are obtained in the moiré band dispersion, and thus the corresponding helical edge state is running along the edge of the moiré-scale lattice system [Fig. 7(c)]. As we have seen, the moiré-scale edge state is partially made from the ring-shaped edge state on the domain boundary around the AB-stacking area (let us say atomic-scale helical edge state). Therefore, we can say the moiré edge state is "edge state from edge state" [Fig. 7(c)], and this is a characteristic phenomenon that is observed in twisted bilayer $Bi_2(Te_{1-x}Se_x)_3$. These topological properties also have twist angle dependence. In the small-angle limit, more edge-state-originated nearly flat bands appear around the Fermi level due to the band folding with the small moiré BZ, as seen in Fig. 5. Therefore, as twist angle is decreased, topological phase transitions occur on VB8 and VB9 and eventually they become topologically trivial bands. The topological phase transition goes through a gap closing at general momenta as described in a general theory of topological phase transitions in 2D systems [55,56] (see Appendixes E and F for more detail). From this perspective, when the twist angle gets smaller, topological bands tend to appear in lower- (or higher-) energy bands.

The edge-state-originated nearly flat bands, moiré-scale edge states, and other properties obtained in twisted bilayer $Bi_2(Te_{1-x}Se_x)_3$ are also reproduced in a more simplified model that we propose: twisted Bernevig-Hughes-Zhang model (see Appendix G). This fact not only allows us to easily explore the properties of these systems, but also indicates that our essential strategy can be applied to other topological materials.

VI. DISCUSSION

In conclusion, we have theoretically studied the electronic structure of twisted bilayer $Bi_2(Te_{1-x}Se_x)_3$. It is revealed that twisted bilayer $Bi_2(Te_{1-x}Se_x)_3$ has a topological insulator domain and a normal insulator domain in the moiré unit cell due to the stacking modulation of the moiré superlattice structure. We have obtained a moiré-scale band inversion and corresponding edge states that are made from the atomic-scale edge state on the domain boundary, thus it can be called "edge state from edge state." With these results, we propose twisted bilayer $Bi_2(Te_{1-x}Se_x)_3$ as a topological moiré material that hosts characteristic low-energy states and multiscale band inversion. This proposal provides a platform to study topological phases both in atomic and moiré scales. In addition, the atomic-scale helical edge states are expected to be used as an ideal platform to realize the Chalker-Coddington network model [57–61] without an external field. The moiré-scale topological states also propose a realization of moiré topological spin Hall materials that do not require external fields. Further, because the wave function of the moiré-scale helical edge state has characteristic density distribution and far larger real-space size than that of helical edge states in previous topological insulator crystals, it allows us to observe the nontriviality of wave function with a real-space observation such as scanning tunneling microscope (STM). While those phenomena proposed by some previous studies require a strong external field [62–68] or a particular symmetry-broken valley setup [28], the role is replaced by the intrinsic strong spin-orbit coupling in twisted bilayer $Bi_2(Te_{1-x}Se_x)_3$. Moreover, twisted bilayer $Bi_2(Te_{1-x}Se_x)_3$ can be a new platform to investigate correlated phases. As shown in the moiré band dispersion, large Rashba splits are predicted around K_M points in our calculation. It indicates that the ratio between bandwidth and the size of the Rashba split can be tuned by changing the twist angle.

Although we have studied a specific material twisted bilayer $Bi_2(Te_{1-x}Se_x)_3$ here, the strategy underlying this study, making a moiré material with a stacking-sensitive topological material, is quite versatile. There is an abundance of stacking-

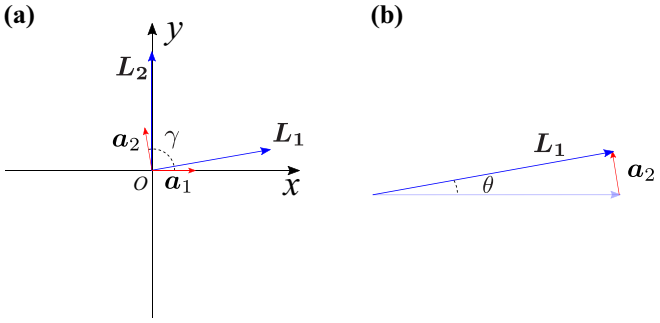

FIG. 8. (a) Atomic lattice vectors $\boldsymbol{a}_1, \boldsymbol{a}_2$ and moiré lattice vectors $\boldsymbol{L}_1, \boldsymbol{L}_2$. (b) Relation between the atomic lattice vector, the moiré lattice vector, and twist angle θ.

sensitive topological materials, and it should be possible to design moiré materials in which multiple topological phase domains coexist with this strategy. The combination of a quantum system with several different topological phase domains and the high tunability of the moiré materials provides an avenue in the search for new quantum materials and devices.

ACKNOWLEDGMENTS

We are grateful to A. Furusaki for fruitful discussion. This work was supported by JST CREST (Grant No. JPMJCR19T2). M.H. was supported by PRESTO, JST (Grant No. JPMJPR21Q6), and JSPS KAKENHI Grant No. 20K14390.

APPENDIX A: MOIRÉ PATTERN

To make a 2D moiré superlattice structure, there are two fundamental methods: lattice constant mismatch and twisting identical lattices. General moiré superlattice systems are made by combining the two methods. In this paper, we focus on the cases of twisting identical lattices.

1. General cases

Generally, given atomic lattice vectors $\boldsymbol{a}_1$, $\boldsymbol{a}_2$, and twist angle θ, the moiré lattice vectors $\boldsymbol{L}_1$ and $\boldsymbol{L}_2$ [Fig. 8(a)] satisfy

$$2\sin\frac{\theta}{2}\boldsymbol{e}_z \times \boldsymbol{L}_1 = -\boldsymbol{a}_2, \quad 2\sin\frac{\theta}{2}\boldsymbol{L}_2 \times \boldsymbol{e}_z = \boldsymbol{a}_1, \tag{A1}$$

within the small-angle approximation [Fig. 8(b)], where $\boldsymbol{e}_z$ is a unit vector along the z axis. By solving these equations, the moiré lattice vectors are obtained as

$$\boldsymbol{L}_1 = \boldsymbol{a}_2 \times \frac{1}{2\sin\frac{\theta}{2}}\boldsymbol{e}_z \approx \boldsymbol{a}_2 \times \frac{1}{\theta}\boldsymbol{e}_z,$$
$$\boldsymbol{L}_2 = \frac{1}{2\sin\frac{\theta}{2}}\boldsymbol{e}_z \times \boldsymbol{a}_1 \approx \frac{1}{\theta}\boldsymbol{e}_z \times \boldsymbol{a}_1. \tag{A2}$$

It is also proved that $\boldsymbol{a}_l$ and $\boldsymbol{L}_m$ satisfy

$$\boldsymbol{a}_l \cdot \boldsymbol{L}_m = \delta_{lm}\frac{|\boldsymbol{a}_1||\boldsymbol{a}_2|}{2\sin\frac{\theta}{2}}\sin\gamma \approx \delta_{lm}\frac{|\boldsymbol{a}_1||\boldsymbol{a}_2|}{\theta}\sin\gamma, \tag{A3}$$

where γ is the angle between $\boldsymbol{a}_1$ and $\boldsymbol{a}_2$.

This relation indicates that the moiré lattice (moiré reciprocal lattice) of the twisted system is similar to the atomic reciprocal lattice (atomic lattice) in the original untwisted system.

2. Trigonal lattice

For a trigonal lattice system, atomic lattice vectors are given with the lattice constant a_0 as

$$\boldsymbol{a}_1 = a_0(1, 0), \quad \boldsymbol{a}_2 = a_0(-1/2, \sqrt{3}/2). \tag{A4}$$

Moiré lattice vectors are given as

$$\boldsymbol{L}_1 = L(\sqrt{3}/2, 1/2), \quad \boldsymbol{L}_2 = L(0, 1), \tag{A5}$$

where the moiré lattice constant L is written as

$$L = \frac{a_0}{2\sin\frac{\theta}{2}}. \tag{A6}$$

Corresponding moiré reciprocal lattice vectors are written as

$$\boldsymbol{G}_1 = \frac{2\pi}{L}\frac{2}{\sqrt{3}}(1, 0), \quad \boldsymbol{G}_3 = \frac{2\pi}{L}\frac{2}{\sqrt{3}}(-1/2, \sqrt{3}/2). \tag{A7}$$

Note that the subscripts follow the definition in Fig. 1(b).

APPENDIX B: EFFECTIVE MODEL OF MOIRÉ SUPERLATTICE SYSTEMS

In this Appendix, we derive a model of a moiré superlattice system. In the following, the atomic lattice constant is set to $a_0 = 1$. In Appendix B 1, we describe the general and exact part of the model derivation that is independent of the detail of the target moiré system. The description in Appendix B 1 is consistent with previous studies [44,45]. In Appendix B 2, we introduce the small-angle approximation, which is generally used in a moiré system. Further, we improve the approximation method of the previous studies to make them more efficient. In Appendix B 3, we describe the system-dependent part of the model derivation. We also make a correction to make the model satisfy symmetry restrictions of the twisted bilayer $Bi_2(Te_{1-x}Se_x)_3$ system.

1. General formula of model derivation

The exact Hamiltonian of a moiré superlattice system is given by the following with a microscopic picture:

$$H = \sum_{\boldsymbol{r}_j}\sum_{\alpha\sigma,\beta'\sigma'}\sum_{pq} t_{pq}^{\alpha\sigma,\beta'\sigma'}(\boldsymbol{r}_j) \times c_{\alpha\sigma}^{\dagger}[\boldsymbol{r}_j + \boldsymbol{d}_{\alpha}(\boldsymbol{r}_j)]c_{\beta'\sigma'}[\boldsymbol{r}_j + \boldsymbol{d}_{\beta'}(\boldsymbol{r}_j) + \boldsymbol{a}_{pq}], \tag{B1}$$

$$\begin{array}{lcl} \boldsymbol{r}_j & : & \text{atomic unit} - \text{cell position}, \\ \alpha\sigma, \beta'\sigma' & : & \text{orbital, spin index}, \\ \boldsymbol{d}_{\alpha,\beta'}(\boldsymbol{r}_j) & : & \text{site position of } \alpha, \beta' \text{ in the unit cell } \boldsymbol{r}_j, \\ pq & : & \text{hopping lattice index } (\boldsymbol{a}_{pq}), \\ c^{\dagger}, c & : & \text{creation/annihilation operator}. \end{array} \tag{B2}$$

Here, $\boldsymbol{r}_j$ is a position of an atomic unit cell, and $\alpha\sigma, \beta'\sigma'$ are indices to specify orbital and spin. Now $\boldsymbol{r}_j$ is defined as the corner of the atomic unit cell, and thus we define $\boldsymbol{d}_{\alpha}(\boldsymbol{r}_j)$ as the site position of the orbital α measured from the corner of the atomic unit cell $\boldsymbol{r}_j$. Due to the effect of twisting,

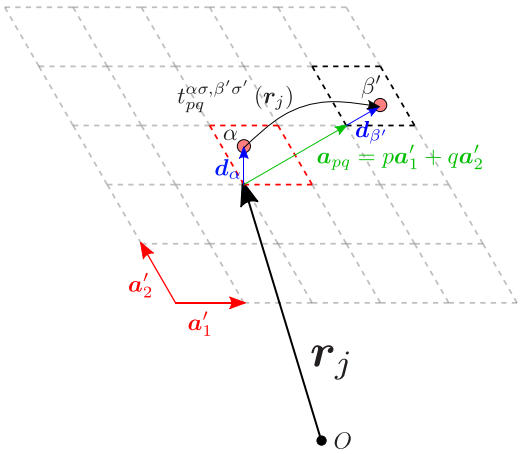

FIG. 9. Definition of the hopping $t_{pq}^{\alpha\sigma,\beta'\sigma'}(\boldsymbol{r}_j)$. $\boldsymbol{r}_j$ is a position that indicates atomic unit-cell index. The $t_{pq}^{\alpha\sigma,\beta'\sigma'}(\boldsymbol{r}_j)$ is a hopping between orbital α spin σ in the atomic unit cell $\boldsymbol{r}_j$ (red dashed cell) and orbital β' spin σ' in the atomic unit cell $\boldsymbol{r}_j + \boldsymbol{a}_{pq}$ (black dashed cell).

$\boldsymbol{d}_\alpha(\boldsymbol{r}_j)$ generally depends on the atomic unit-cell position $\boldsymbol{r}_j$. $c_{\alpha\sigma}^\dagger[\boldsymbol{r}_j + \boldsymbol{d}_\alpha(\boldsymbol{r}_j)]$ is a creation operator of a fermion on the orbital α spin σ in the atomic unit cell $\boldsymbol{r}_j$, and c is an annihilation operator. $t_{pq}^{\alpha\sigma,\beta'\sigma'}(\boldsymbol{r}_j)$ is a hopping parameter which is defined as a hopping between "orbital α spin σ in the atomic unit cell $\boldsymbol{r}_j$" and "orbital β' spin σ' in the atomic unit cell $\boldsymbol{r}_j + \boldsymbol{a}_{pq}$" (Fig. 9). The $\boldsymbol{a}_{pq}$ are defined with integers p, q as

$$\boldsymbol{a}_{pq} = p\boldsymbol{a}_1' + q\boldsymbol{a}_2', \tag{B3}$$

where $\boldsymbol{a}_1'$, $\boldsymbol{a}_2'$ are atomic lattice vectors defined differently in intralayer and interlayer cases. The definitions of $\boldsymbol{a}_1'$ and $\boldsymbol{a}_2'$ are

$$\begin{array}{llll} \boldsymbol{a}_1' = C_{\theta/2}\boldsymbol{a}_1, & \boldsymbol{a}_2' = C_{\theta/2}\boldsymbol{a}_2 & \text{(intralayer, upper layer)}, \\ \boldsymbol{a}_1' = C_{-\theta/2}\boldsymbol{a}_1, & \boldsymbol{a}_2' = C_{-\theta/2}\boldsymbol{a}_2 & \text{(intralayer, lower layer)}, \\ \boldsymbol{a}_1' = \boldsymbol{a}_1, & \boldsymbol{a}_2' = \boldsymbol{a}_2 & \text{(interlayer)}. \end{array} \tag{B4}$$

We assume that long-range hoppings are negligible and $\sum_{pq}$ is a finite sum. There are two points to note about $\boldsymbol{a}_{pq}$ and $\sum_{pq}$. First, in the interlayer case, $(\boldsymbol{a}_1, \boldsymbol{a}_2)$ does not match either the atomic lattice period of the upper layer or that of the lower layer. As a result, it can be possible that there is no β' site (or there are two β' sites) in the atomic unit cell $\boldsymbol{r}_j + \boldsymbol{a}_{pq}$. However, because the small-angle limit is interpreted as a continuous limit, those inconvenient cases are neglected. Second, because $\boldsymbol{d}_\alpha(\boldsymbol{r}_j)$ depends on the position in the moiré unit cell $\boldsymbol{r}_j$, a site can disappear on one end of the summation range of $\sum_{pq}$ and appear on the other end when $\boldsymbol{r}_j$ is changed. This will essentially make a "discontinuity" in the Hamiltonian. However, as long as the range of $\sum_{pq}$ is large enough, the disappearing and appearing hoppings have small absolute values and thus the discontinuity is negligible.

We perform a Fourier transform of Eq. (B1). We assume that the Wannier functions are independent of position in the moiré unit cell, and thus the annihilation operator is transformed as

$$c_{\alpha\sigma}(\boldsymbol{r}_j) = \int d\boldsymbol{k}\, e^{i\boldsymbol{k}\cdot\boldsymbol{r}_j} c_{\alpha\sigma,\boldsymbol{k}}. \tag{B5}$$

The Fourier transform of Eq. (B1) is obtained as

$$\begin{aligned} H = \int d\boldsymbol{k}\, d\boldsymbol{k}' \sum_{\boldsymbol{r}_j} \sum_{\alpha\sigma,\beta'\sigma'} & \\ \times \left[\sum_{pq} t_{pq}^{\alpha\sigma,\beta'\sigma'}(\boldsymbol{r}_j) e^{-i\boldsymbol{k}\cdot\boldsymbol{d}_\alpha(\boldsymbol{r}_j)} e^{i\boldsymbol{k}'\cdot(\boldsymbol{d}_{\beta'}(\boldsymbol{r}_j)+\boldsymbol{a}_{pq})} \right] & \\ \times e^{i(-\boldsymbol{k}'+\boldsymbol{k})\boldsymbol{r}_j} c_{\alpha\sigma,\boldsymbol{k}}^\dagger c_{\beta'\sigma',\boldsymbol{k}'}. & \end{aligned} \tag{B6}$$

We focus on the bracketed part. The $\boldsymbol{d}_\alpha(\boldsymbol{r}_j)$ and $t_{pq}^{\alpha\sigma,\beta'\sigma'}(\boldsymbol{r}_j)$ are moiré periodic. Therefore, the bracketed part is moiré periodic and can be decomposed into components of the moiré reciprocal lattice vectors $\boldsymbol{G}_l$ as

$$\begin{aligned} \left[\sum_{pq} t_{pq}^{\alpha\sigma,\beta'\sigma'}(\boldsymbol{r}_j) e^{-i\boldsymbol{k}\cdot\boldsymbol{d}_\alpha(\boldsymbol{r}_j)} e^{i\boldsymbol{k}'\cdot(\boldsymbol{d}_{\beta'}(\boldsymbol{r}_j)+\boldsymbol{a}_{pq})} \right] & \\ = \sum_{\boldsymbol{G}_l} e^{i\boldsymbol{G}_l\cdot\boldsymbol{r}_j} t_{\boldsymbol{k},\boldsymbol{k}',\boldsymbol{G}_l}^{\alpha\sigma,\beta'\sigma'}, & \end{aligned} \tag{B7}$$

where $t_{\boldsymbol{k},\boldsymbol{k}',\boldsymbol{G}_l}^{\alpha\sigma,\beta'\sigma'}$ is the Fourier transform of the bracketed part. Note that the $t_{\boldsymbol{k},\boldsymbol{k}',\boldsymbol{G}_l}^{\alpha\sigma,\beta'\sigma'}$ is not the Fourier transform of $t_{pq}^{\alpha\sigma,\beta'\sigma'}(\boldsymbol{r}_j)$ because the bracketed part includes a sum on p, q and phase factors.

By using Eq. (B7), the Hamiltonian is written as

$$\begin{aligned} H &= \int d\boldsymbol{k}\, d\boldsymbol{k}' \sum_{\boldsymbol{r}_j} \sum_{\alpha\sigma,\beta'\sigma'} \sum_{\boldsymbol{G}_l} t_{\boldsymbol{k},\boldsymbol{k}',\boldsymbol{G}_l}^{\alpha\sigma,\beta'\sigma'} e^{i(-\boldsymbol{k}+\boldsymbol{k}'+\boldsymbol{G}_l)\cdot\boldsymbol{r}_j} c_{\alpha\sigma,\boldsymbol{k}}^\dagger c_{\beta'\sigma',\boldsymbol{k}'} \\ &= \int d\boldsymbol{k} \sum_{\alpha\sigma,\beta'\sigma'} \sum_{\boldsymbol{G}_l} t_{\boldsymbol{k},\boldsymbol{k}-\boldsymbol{G}_l,\boldsymbol{G}_l}^{\alpha\sigma,\beta'\sigma'} c_{\alpha\sigma,\boldsymbol{k}}^\dagger c_{\beta'\sigma',\boldsymbol{k}-\boldsymbol{G}_l}. \end{aligned} \tag{B8}$$

Note that $\boldsymbol{k}'$ is restricted to $\boldsymbol{k} - \boldsymbol{G}_l$.

So far, the model derivation is exact and general. However, in Eq. (B7), all $t_{pq}^{\alpha\sigma,\beta'\sigma'}(\boldsymbol{r}_j)$ in the moiré unit cell are needed to obtain exact value of $t_{\boldsymbol{k},\boldsymbol{k}',\boldsymbol{G}_l}^{\alpha\sigma,\beta'\sigma'}$. Because it is usually unrealistic, we use a small-angle approximations to obtain $t_{\boldsymbol{k},\boldsymbol{k}',\boldsymbol{G}_l}^{\alpha\sigma,\beta'\sigma'}$, as described in the following.

2. Small-angle approximation

In a small twist angle case, $t_{\boldsymbol{k},\boldsymbol{k}',\boldsymbol{G}_l}^{\alpha\sigma,\beta'\sigma'}$ can be approximately obtained as following. First, we obtain $t_{pq}^{\alpha\sigma,\beta'\sigma'}(\boldsymbol{r}_j)$ at finite number of sampling points $\{\boldsymbol{r}_j\}$ in the moiré unit cell. In a small twist angle case, the local atomic lattice structures around each sampling point can be approximated by untwisted atomic lattices with proper layer-stacking orders. We perform first-principles calculation for each untwisted structure and use the results as approximate value of $t_{pq}^{\alpha\sigma,\beta'\sigma'}(\boldsymbol{r}_j)$ at the sampling points. With the approximated $t_{pq}^{\alpha\sigma,\beta'\sigma'}(\boldsymbol{r}_j)$, $t_{\boldsymbol{k},\boldsymbol{k}',\boldsymbol{G}_l}^{\alpha\sigma,\beta'\sigma'}$ are obtained by the discrete Fourier transform (B7).

Generally, the discrete Fourier transform guarantees that the parameters in the sampling points are reproduced, but those in the intermediate area are not necessarily estimated in a physically reasonable way. To obtain a reasonable estimation for the whole moiré unit cell by discrete Fourier transform, we need to adopt appropriate $\boldsymbol{G}_l$, and sampling points must be determined to capture the "feature values," for

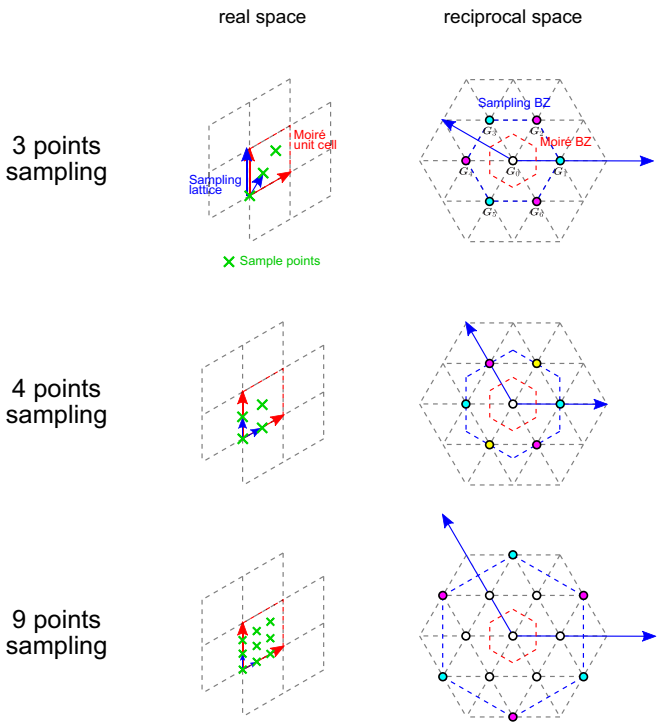

FIG. 10. Examples of parameter sampling and $\boldsymbol{G}_l$ adopted in the discrete Fourier transform in a trigonal lattice system. The left figure shows the moiré unit cell (red), sampling points, and sampling lattice vectors (blue arrows) in the real space. The right figure shows the moiré BZ (red dashed), reciprocal vectors of the sampling lattice (blue arrows), and $\boldsymbol{G}_l$ adopted in the discrete Fourier transform (white and colored dots). For $\boldsymbol{G}_l$ shown with the same colored dot, $t^{\alpha\sigma,\beta'\sigma'}_{\boldsymbol{k},\boldsymbol{k}',\boldsymbol{G}_l}$ have the same value.

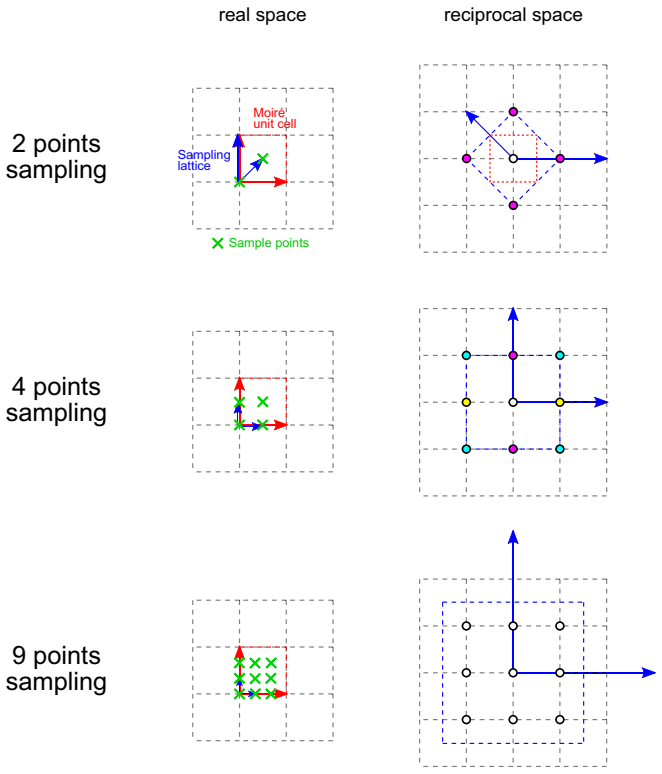

FIG. 11. Examples of parameter sampling and $\boldsymbol{G}_l$ adopted in the discrete Fourier transform in a square-lattice system. The left figure shows the moiré unit cell (red), sampling points, and sampling lattice vectors (blue arrows) in the real space. The right figure shows the moiré BZ (red dashed), reciprocal vectors of the sampling lattice (blue arrows), and $\boldsymbol{G}_l$ adopted in the discrete Fourier transform (white and colored dots). For $\boldsymbol{G}_l$ shown with the same colored dot, $t^{\alpha\sigma,\beta'\sigma'}_{\boldsymbol{k},\boldsymbol{k}',\boldsymbol{G}_l}$ have the same value.

example, the maximum and minimum values of $t^{\alpha\sigma,\beta'\sigma'}_{pq}(\boldsymbol{r}_j)$. Therefore, the sampling points should be determined from the atomic positions in the untwisted atomic lattice. Here, we explain a general way to decide the sampling points and how to choose $\boldsymbol{G}_l$ in detail, and then we show some examples in Figs. 10 and 11. As the first step, we decide untwisted bilayer structures with interlayer in-plane shift $\{\Delta\boldsymbol{r}_j\}$ that should be sampled. For the convenience of the discrete Fourier transform, the list $\{\Delta\boldsymbol{r}_j\}$ should be taken as a mesh in the atomic unit cell. As explained above, the $\{\Delta\boldsymbol{r}_j\}$ should include the cases where feature values are obtained. Typically, the $\{\Delta\boldsymbol{r}_j\}$ include the cases where the atoms on the upper layer and the lower layer are closest or farthest. We translate the $\{\Delta\boldsymbol{r}_j\}$ to a position in the moiré unit cell $\{\boldsymbol{r}_j\}$ by using the equation $\Delta\boldsymbol{r}_j = \boldsymbol{r}_j \times \theta\boldsymbol{e}_z$ [easily obtained from Fig. 8(b)]. As a result, a sampling lattice (green crosses and blue arrows in left figures in Figs. 10 and 11) is obtained in the moiré unit cell and a sampling BZ is also defined in the reciprocal space (blue hexagons in the right figures). The number of sampling points (the number of $\Delta\boldsymbol{r}_j$, originally) decides a number of $\boldsymbol{G}_l$ that are taken into account in Eqs. (B7) and (B8). Moiré reciprocal lattice points included in the sampling BZ (white dots) are adopted as $\boldsymbol{G}_l$. Additionally, moiré reciprocal lattice points on the boundary of the sampling BZ (cyan, magenta, and yellow dots) are also adopted as $\boldsymbol{G}_l$, but we assume that $t^{\alpha\sigma,\beta'\sigma'}_{\boldsymbol{k},\boldsymbol{k}',\boldsymbol{G}_l}$ have same value in the points that are connected by the reciprocal vectors of the sampling lattice (blue arrows in the right figures). $\boldsymbol{G}_l$ outside of the sampling BZ are neglected, i.e., components with frequencies higher than the sampling points are neglected. By using this method, the number of the sampling points and $\boldsymbol{G}_l$ are equal, and thus $t^{\alpha\sigma,\beta'\sigma'}_{\boldsymbol{k},\boldsymbol{k}',\boldsymbol{G}_l}$ are uniquely determined by the discrete Fourier transform (B7). Examples of the way to choose $\boldsymbol{G}_l$ are shown in Figs. 10 and 11 (for trigonal and square cases, respectively). In each row, the left figure is the moiré lattice in the real space, and the right figure is the moiré reciprocal lattice in the reciprocal space. In the left figure, the moiré unit cell (red) and sampling points (green crosses) are shown. Blue arrows are basic lattice vectors of the sampling lattice. In the right figure, the moiré BZ (red dashed) and the sampling BZ (blue dashed), which are defined by the sampling lattice vectors, are shown. Moiré reciprocal lattice points that are adopted as $\boldsymbol{G}_l$ are shown with dots. If it is included in the sampling BZ, the dot is white. If it is on the boundary of the sampling BZ, the dot is colored (cyan, magenta, or yellow) and the points that are connected by the reciprocal vectors of the sampling lattice (blue arrows) have the same color. $t^{\alpha\sigma,\beta'\sigma'}_{\boldsymbol{k},\boldsymbol{k}',\boldsymbol{G}_l}$ on those $\boldsymbol{G}_l$ have the same value. For example, in the case of the three points sampling in Fig. 10,

$$t^{\alpha\sigma,\beta'\sigma'}_{\boldsymbol{k},\boldsymbol{k}',\boldsymbol{G}_1} = t^{\alpha\sigma,\beta'\sigma'}_{\boldsymbol{k},\boldsymbol{k}',\boldsymbol{G}_3} = t^{\alpha\sigma,\beta'\sigma'}_{\boldsymbol{k},\boldsymbol{k}',\boldsymbol{G}_5}. \tag{B9}$$

Note that the number of the sampling points in the left figure equals to the number of $\boldsymbol{G}_l$ in the right figure (dots with same color on the boundary should be counted as one) in each column.

Note that depending on the symmetry of the system and the center of momentum of the cutoff (see Appendix C 2), hopping parameters in some stacking orders can be fixed to be 0 [69].

3. Specific formula for $Bi_2(Te_{1-x}Se_x)_3$

Here, we apply the method given in the previous subsection to $Bi_2(Te_{1-x}Se_x)_3$. In the case of $Bi_2(Te_{1-x}Se_x)_3$, the in-plane atomic positions are only three in the atomic unit cell (C_3-symmetry centers). Therefore, the simplest choice is to calculate three untwisted stacking structures (the three points sampling in Fig. 10). Here, we define the three stacking orders as AA, AB, and AC stacking. In this case, we take components of seven $\boldsymbol{G}_l$,

$$\boldsymbol{G}_l = \{\boldsymbol{G}_0, \boldsymbol{G}_1, \boldsymbol{G}_2, \boldsymbol{G}_3, \boldsymbol{G}_4, \boldsymbol{G}_5, \boldsymbol{G}_6\}, \tag{B10}$$

and assume equivalences between them as

$$t^{\alpha\sigma,\beta'\sigma'}_{\boldsymbol{k},\boldsymbol{k}',\boldsymbol{G}_1} = t^{\alpha\sigma,\beta'\sigma'}_{\boldsymbol{k},\boldsymbol{k}',\boldsymbol{G}_3} = t^{\alpha\sigma,\beta'\sigma'}_{\boldsymbol{k},\boldsymbol{k}',\boldsymbol{G}_5}, \quad t^{\alpha\sigma,\beta'\sigma'}_{\boldsymbol{k},\boldsymbol{k}',\boldsymbol{G}_2} = t^{\alpha\sigma,\beta'\sigma'}_{\boldsymbol{k},\boldsymbol{k}',\boldsymbol{G}_4} = t^{\alpha\sigma,\beta'\sigma'}_{\boldsymbol{k},\boldsymbol{k}',\boldsymbol{G}_6}. \tag{B11}$$

Including a completely independent component

$$t^{\alpha\sigma,\beta'\sigma'}_{\boldsymbol{k},\boldsymbol{k}',\boldsymbol{G}_0}, \tag{B12}$$

the degree of freedom is three, which is the same as the number of the sampling points. Therefore, using the relation (B11), we can determine the seven $t^{\alpha\sigma,\beta'\sigma'}_{\boldsymbol{k},\boldsymbol{k}',\boldsymbol{G}_l}$ from the three sampling points with the discrete Fourier transform.

The hopping parameters in the three sampling points, $t^{\alpha\sigma,\beta'\sigma'}_{pq}(\boldsymbol{r}_{AA})$, $t^{\alpha\sigma,\beta'\sigma'}_{pq}(\boldsymbol{r}_{AB})$, and $t^{\alpha\sigma,\beta'\sigma'}_{pq}(\boldsymbol{r}_{AC})$, are calculated with the first-principles calculation of untwisted structures. However, when the hopping parameters of the twisted structure are estimated from untwisted structures, the Hamiltonian (B8) will break the Hermitian and C_{3z} symmetries slightly. Therefore, we add a correction factor in Eq. (B7).

The restrictions by each symmetry are given as following. The detail of the derivation of the restrictions is given in Appendix B 3 b. The Hermitian symmetry restriction is

$$t^{\alpha\sigma,\beta'\sigma'}_{\boldsymbol{k}+\boldsymbol{G}_l,\boldsymbol{k},\boldsymbol{G}_l}{}^{*} = t^{\beta'\sigma',\alpha\sigma}_{\boldsymbol{k},\boldsymbol{k}+\boldsymbol{G}_l,-\boldsymbol{G}_l} \tag{B13}$$

and the C_{3z}-symmetry restriction is

$$t^{\alpha\sigma,\beta'\sigma'}_{\boldsymbol{k},\boldsymbol{k}-\boldsymbol{G}_l,\boldsymbol{G}_l} = t^{\widetilde{\alpha\sigma},\widetilde{\beta'\sigma'}}_{C_3\boldsymbol{k},C_3\boldsymbol{k}-C_3\boldsymbol{G}_l,C_3\boldsymbol{G}_l}, \tag{B14}$$

where the orbital-spin index $\widetilde{\alpha\sigma}$ means the C_{3z} rotated orbital spin. The twisted structure also has time-reversal symmetry and its restriction is

$$(-1)^{1-\delta_{\alpha\sigma'}}\, t^{\alpha\sigma,\beta'\sigma'}_{-\boldsymbol{k},-\boldsymbol{k}-\boldsymbol{G}_l,\boldsymbol{G}_l}{}^{*} = t^{\alpha\bar{\sigma},\beta'\bar{\sigma}'}_{\boldsymbol{k},\boldsymbol{k}+\boldsymbol{G}_l,-\boldsymbol{G}_l}, \tag{B15}$$

where $\bar{\sigma}$ means the opposite spin, but this equation is satisfied when the three untwisted structures have the time-reversal symmetry.

To satisfy these equations, we add a correction factor $e^{i\frac{\boldsymbol{G}_m}{2}\cdot(\boldsymbol{d}_\alpha(\boldsymbol{r}_j)+\boldsymbol{d}_{\beta'}(\boldsymbol{r}_j)+\boldsymbol{a}_{pq})}$ in Eq. (B7) as

$$\begin{aligned}\sum_{\boldsymbol{G}_l} e^{i\boldsymbol{G}_l\cdot\boldsymbol{r}_j}\, t^{\alpha\sigma,\beta'\sigma'}_{\boldsymbol{k},\boldsymbol{k}-\boldsymbol{G}_m,\boldsymbol{G}_l} &= \left[\sum_{pq} t^{\alpha\sigma,\beta'\sigma'}_{pq}(\boldsymbol{r}_j) e^{-i\boldsymbol{k}\cdot\boldsymbol{d}_\alpha(\boldsymbol{r}_j)} e^{i(\boldsymbol{k}-\boldsymbol{G}_m)\cdot(\boldsymbol{d}_{\beta'}(\boldsymbol{r}_j)+\boldsymbol{a}_{pq})} e^{i\frac{\boldsymbol{G}_m}{2}\cdot(\boldsymbol{d}_\alpha(\boldsymbol{r}_j)+\boldsymbol{d}_{\beta'}(\boldsymbol{r}_j)+\boldsymbol{a}_{pq})}\right] \\ &= \left[\sum_{pq} t^{\alpha\sigma,\beta'\sigma'}_{pq}(\boldsymbol{r}_j) e^{i(\boldsymbol{k}-\frac{\boldsymbol{G}_m}{2})\cdot(-\boldsymbol{d}_\alpha(\boldsymbol{r}_j)+\boldsymbol{d}_{\beta'}(\boldsymbol{r}_j)+\boldsymbol{a}_{pq})}\right] \\ &= h^{\alpha\sigma,\beta'\sigma'}_{\boldsymbol{r}_j}(\boldsymbol{k}-\boldsymbol{G}_m/2).\end{aligned} \tag{B16}$$

Because the correction factor tends to 1 as the twist angle gets small, this correction is reasonable. Note that the right-hand side $h^{\alpha\sigma,\beta'\sigma'}_{\boldsymbol{r}_j}(\boldsymbol{k}-\boldsymbol{G}_m/2)$ is basically the matrix element of the Hamiltonian with momentum $\boldsymbol{k}-\boldsymbol{G}_m/2$ given by the parameters of untwisted structure around $\boldsymbol{r}_j$. The only difference is the momentum twisting due to the different definition of $\boldsymbol{a}'_{1,2}$ in Eq. (B4). The explicit definition is given as, for $\alpha\sigma, \beta'\sigma' \in$ upper layer,

$$h^{\alpha\sigma,\beta'\sigma'}_{\boldsymbol{r}_j}(\boldsymbol{k}-\boldsymbol{G}_m/2) = \sum_{pq} t^{\alpha\sigma,\beta'\sigma'}_{\mathrm{DFT},pq}(\boldsymbol{r}_j)\, e^{iC_{-\theta/2}(\boldsymbol{k}-\boldsymbol{G}_m/2)\cdot(-\boldsymbol{d}_\alpha(\boldsymbol{r}_j)+\boldsymbol{d}_{\beta'}(\boldsymbol{r}_j)+\boldsymbol{a}_{pq})}, \tag{B17}$$

for $\alpha\sigma, \beta'\sigma' \in$ lower layer,

$$h^{\alpha\sigma,\beta'\sigma'}_{\boldsymbol{r}_j}(\boldsymbol{k}-\boldsymbol{G}_m/2) = \sum_{pq} t^{\alpha\sigma,\beta'\sigma'}_{\mathrm{DFT},pq}(\boldsymbol{r}_j)\, e^{iC_{\theta/2}(\boldsymbol{k}-\boldsymbol{G}_m/2)\cdot(-\boldsymbol{d}_\alpha(\boldsymbol{r}_j)+\boldsymbol{d}_{\beta'}(\boldsymbol{r}_j)+\boldsymbol{a}_{pq})}, \tag{B18}$$

for $\alpha\sigma \in$ upper layer and $\beta'\sigma' \in$ lower layer,

$$h^{\alpha\sigma,\beta'\sigma'}_{\boldsymbol{r}_j}(\boldsymbol{k}-\boldsymbol{G}_m/2) = \sum_{pq} t^{\alpha\sigma,\beta'\sigma'}_{\mathrm{DFT},pq}(\boldsymbol{r}_j)\, e^{i(\boldsymbol{k}-\boldsymbol{G}_m/2)\cdot(-\boldsymbol{d}_\alpha(\boldsymbol{r}_j)+\boldsymbol{d}_{\beta'}(\boldsymbol{r}_j)+\boldsymbol{a}_{pq})}, \quad h^{\beta'\sigma',\alpha\sigma}_{\boldsymbol{r}_j}(\boldsymbol{k}-\boldsymbol{G}_m/2) = h^{\alpha\sigma,\beta'\sigma'}_{\boldsymbol{r}_j}(\boldsymbol{k}-\boldsymbol{G}_m/2)^{\dagger}, \tag{B19}$$

where $t^{\alpha\sigma,\beta'\sigma'}_{\mathrm{DFT},pq}(\boldsymbol{r}_j)$ is the hopping parameter of the untwisted structure around $\boldsymbol{r}_j$ calculated by the first-principles calculation.

The discrete Fourier transform is performed as

$$
\begin{aligned}
t^{\alpha\sigma,\beta'\sigma'}_{\boldsymbol{k},\boldsymbol{k},\boldsymbol{G}_0} &= \frac{1}{3}\left[h^{\alpha\sigma,\beta'\sigma'}_{\boldsymbol{r}_{AA}}(\boldsymbol{k}) + h^{\alpha\sigma,\beta'\sigma'}_{\boldsymbol{r}_{AB}}(\boldsymbol{k}) + h^{\alpha\sigma,\beta'\sigma'}_{\boldsymbol{r}_{AC}}(\boldsymbol{k})\right], \\
t^{\alpha\sigma,\beta'\sigma'}_{\boldsymbol{k},\boldsymbol{k}-\boldsymbol{G}_l,\boldsymbol{G}_l} &= \frac{1}{9}\left[h^{\alpha\sigma,\beta'\sigma'}_{\boldsymbol{r}_{AA}}(\boldsymbol{k}-\boldsymbol{G}_l/2) + e^{-i\frac{2\pi}{3}} h^{\alpha\sigma,\beta'\sigma'}_{\boldsymbol{r}_{AB}}(\boldsymbol{k}-\boldsymbol{G}_l/2) + e^{i\frac{2\pi}{3}} h^{\alpha\sigma,\beta'\sigma'}_{\boldsymbol{r}_{AC}}(\boldsymbol{k}-\boldsymbol{G}_l/2)\right] \ (l=1,3,5), \\
t^{\alpha\sigma,\beta'\sigma'}_{\boldsymbol{k},\boldsymbol{k}-\boldsymbol{G}_l,\boldsymbol{G}_l} &= \frac{1}{9}\left[h^{\alpha\sigma,\beta'\sigma'}_{\boldsymbol{r}_{AA}}(\boldsymbol{k}-\boldsymbol{G}_l/2) + e^{i\frac{2\pi}{3}} h^{\alpha\sigma,\beta'\sigma'}_{\boldsymbol{r}_{AB}}(\boldsymbol{k}-\boldsymbol{G}_l/2) + e^{-i\frac{2\pi}{3}} h^{\alpha\sigma,\beta'\sigma'}_{\boldsymbol{r}_{AC}}(\boldsymbol{k}-\boldsymbol{G}_l/2)\right] \ (l=2,4,6). \qquad \text{(B20)}
\end{aligned}
$$

With these definitions, Eqs. (B11), (B13), (B14), and (B15) are satisfied. The $t^{\alpha\sigma,\beta'\sigma'}_{\boldsymbol{k},\boldsymbol{k},\boldsymbol{G}_0}$ term can be understood as an averaged term, and the others as moiré modulation terms.

a. Gauge selection

In Eqs. (B17)–(B19), the phase factors are calculated with the explicit difference of the orbital positions. There is another standard way to calculate the phase factor, where a phase of the basic translations is given only to intercell hopping terms. In an untwisted system, these two are connected by a gauge transform, and thus have no physical difference. However, in a moiré system, they are physically different in a strict sense due to the interpolation of the Hamiltonian. Although the difference is negligible in the small-angle limit with a small cutoff momentum, the former gives a better interpolation for the large-$\boldsymbol{k}$ region. Therefore, the former definition is recommended, as we used.

b. Derivation of symmetry restrictions

We start from the Hamiltonian (B1):

$$
H = \sum_{\boldsymbol{r}_j}\sum_{\alpha\sigma,\beta'\sigma'}\sum_{pq} t^{\alpha\sigma,\beta'\sigma'}_{pq}(\boldsymbol{r}_j)\, c^\dagger_{\alpha\sigma}[\boldsymbol{r}_j + \boldsymbol{d}_\alpha(\boldsymbol{r}_j)] c_{\beta'\sigma'}[\boldsymbol{r}_j + \boldsymbol{d}_{\beta'}(\boldsymbol{r}_j) + \boldsymbol{a}_{pq}]. \qquad \text{(B21)}
$$

(i) Hermitian symmetry. The Hermite conjugate of the Hamiltonian is given as

$$
\begin{aligned}
H^\dagger &= \sum_{\boldsymbol{r}_j}\sum_{\alpha\sigma,\beta'\sigma'}\sum_{pq} t^{\alpha\sigma,\beta'\sigma'\,*}_{pq}(\boldsymbol{r}_i)\, c^\dagger_{\beta'\sigma'}(\boldsymbol{r}_j + \boldsymbol{d}_{\beta'}(\boldsymbol{r}_j) + \boldsymbol{a}_{pq}) c_{\alpha\sigma}[\boldsymbol{r}_j + \boldsymbol{d}_\alpha(\boldsymbol{r}_j)] \\
&= \int d\boldsymbol{k}\, d\boldsymbol{k}' \sum_{\boldsymbol{r}_j}\sum_{\alpha\sigma,\beta'\sigma'}\left[\sum_{pq} t^{\alpha\sigma,\beta'\sigma'}_{pq}(\boldsymbol{r}_j) e^{-i\boldsymbol{k}'\cdot\boldsymbol{d}_\alpha(\boldsymbol{r}_j)} e^{i\boldsymbol{k}\cdot(\boldsymbol{d}_{\beta'}(\boldsymbol{r}_j)+\boldsymbol{a}_{pq})}\right]^* e^{i(-\boldsymbol{k}+\boldsymbol{k}')\cdot\boldsymbol{r}_j}\, c^\dagger_{\beta'\sigma',\boldsymbol{k}} c_{\alpha\sigma,\boldsymbol{k}'} \\
&= \int d\boldsymbol{k}\, d\boldsymbol{k}' \sum_{\boldsymbol{r}_j}\sum_{\alpha\sigma,\beta'\sigma'}\sum_{\boldsymbol{G}_l} e^{-i\boldsymbol{G}_l\cdot\boldsymbol{r}_j} t^{\alpha\sigma,\beta'\sigma'\,*}_{\boldsymbol{k}',\boldsymbol{k},\boldsymbol{G}_l} e^{i(-\boldsymbol{k}+\boldsymbol{k}')\cdot\boldsymbol{r}_j}\, c^\dagger_{\beta'\sigma',\boldsymbol{k}} c_{\alpha\sigma,\boldsymbol{k}'} \\
&= \int d\boldsymbol{k} \sum_{\alpha\sigma,\beta'\sigma'}\sum_{\boldsymbol{G}_l} t^{\alpha\sigma,\beta'\sigma'}_{\boldsymbol{k}+\boldsymbol{G}_l,\boldsymbol{k},\boldsymbol{G}_l\,*} c^\dagger_{\beta'\sigma',\boldsymbol{k}} c_{\alpha\sigma,\boldsymbol{k}+\boldsymbol{G}_l}. \qquad \text{(B22)}
\end{aligned}
$$

The conditions for this to be Hermite [Eq. (B13)] are

$$
t^{\alpha\sigma,\beta'\sigma'}_{\boldsymbol{k}+\boldsymbol{G}_l,\boldsymbol{k},\boldsymbol{G}_l\,*} = t^{\beta'\sigma',\alpha\sigma}_{\boldsymbol{k},\boldsymbol{k}+\boldsymbol{G}_l,-\boldsymbol{G}_l}. \qquad \text{(B23)}
$$

When the Hamiltonian of the untwisted structures are Hermite,

$$
h^{\alpha\sigma,\beta'\sigma'}_{\boldsymbol{r}}(\boldsymbol{k})^* = h^{\beta'\sigma',\alpha\sigma}_{\boldsymbol{r}}(\boldsymbol{k}) \qquad \text{(B24)}
$$

is satisfied and Eq. (B13) is satisfied by using Eq. (B20).

(ii) C_{3z} symmetry. The C_3-rotated Hamiltonian is

$$
\begin{aligned}
C_3 H C_3^\dagger &= \sum_{\boldsymbol{r}_j}\sum_{\alpha\sigma,\beta'\sigma'}\sum_{pq} t^{\alpha\sigma,\beta'\sigma'}_{pq}(\boldsymbol{r}_j)\, c^\dagger_{\widetilde{\alpha\sigma}}[C_3\boldsymbol{r}_j + C_3\boldsymbol{d}_\alpha(\boldsymbol{r}_j)] c_{\widetilde{\beta'\sigma'}}[C_3\boldsymbol{r}_j + C_3\boldsymbol{a}_{pq} + C_3\boldsymbol{d}_{\beta'}(\boldsymbol{r}_j)] \\
&= \int d\boldsymbol{k}\, d\boldsymbol{k}' \sum_{\boldsymbol{r}_j}\sum_{\alpha\sigma,\beta'\sigma'}\left[\sum_{pq} t^{\alpha\sigma,\beta'\sigma'}_{pq}(\boldsymbol{r}_j) e^{-iC_3^{-1}\boldsymbol{k}\cdot\boldsymbol{d}_\alpha(\boldsymbol{r}_j)} e^{iC_3^{-1}\boldsymbol{k}'\cdot(\boldsymbol{d}_{\beta'}(\boldsymbol{r}_j)+\boldsymbol{a}_{pq})}\right] e^{iC_3^{-1}(-\boldsymbol{k}+\boldsymbol{k}')\cdot\boldsymbol{r}_j} c^\dagger_{\widetilde{\alpha\sigma},\boldsymbol{k}} c_{\widetilde{\beta'\sigma'},\boldsymbol{k}'} \\
&= \int d\boldsymbol{k}\, d\boldsymbol{k}' \sum_{\boldsymbol{r}_j}\sum_{\alpha\sigma,\beta'\sigma'}\left[\sum_{\boldsymbol{G}_l} e^{i\boldsymbol{G}_l\cdot\boldsymbol{r}_j} t^{\alpha\sigma,\beta'\sigma'}_{C_3^{-1}\boldsymbol{k},C_3^{-1}\boldsymbol{k}',\boldsymbol{G}_l}\right] e^{iC_3^{-1}(-\boldsymbol{k}+\boldsymbol{k}')\cdot\boldsymbol{r}_j} c^\dagger_{\widetilde{\alpha\sigma},\boldsymbol{k}} c_{\widetilde{\beta'\sigma'},\boldsymbol{k}'}
\end{aligned}
$$

$$= \int d\boldsymbol{k} \sum_{\alpha\sigma,\beta'\sigma'} \sum_{\boldsymbol{G}_l} t^{\alpha\sigma,\beta'\sigma'}_{C_3^{-1}\boldsymbol{k},C_3^{-1}\boldsymbol{k}-\boldsymbol{G}_l,\boldsymbol{G}_l} \, c^\dagger_{\widetilde{\alpha\sigma},\boldsymbol{k}} c_{\widetilde{\beta'\sigma'},\boldsymbol{k}-C_3\boldsymbol{G}_l}$$

$$= \int d\boldsymbol{k} \sum_{\alpha\sigma,\beta'\sigma'} \sum_{\boldsymbol{G}_l} t^{\alpha\sigma,\beta'\sigma'}_{\boldsymbol{k},\boldsymbol{k}-\boldsymbol{G}_l,\boldsymbol{G}_l} \, c^\dagger_{\widetilde{\alpha\sigma},C_3\boldsymbol{k}} c_{\widetilde{\beta'\sigma'},C_3\boldsymbol{k}-C_3\boldsymbol{G}_l}, \tag{B25}$$

where the orbital-spin index $\widetilde{\alpha\sigma}$ means the C_{3z}-rotated orbital spin. The conditions for this to be C_3 symmetric [Eq. (B14)] are

$$t^{\alpha\sigma,\beta'\sigma'}_{\boldsymbol{k},\boldsymbol{k}-\boldsymbol{G}_l,\boldsymbol{G}_l} = t^{\widetilde{\alpha\sigma},\widetilde{\beta'\sigma'}}_{C_3\boldsymbol{k},C_3\boldsymbol{k}-C_3\boldsymbol{G}_l,C_3\boldsymbol{G}_l}. \tag{B26}$$

When the Hamiltonian of the untwisted structures are C_3 symmetric,

$$h^{\alpha\sigma,\beta'\sigma'}_{\boldsymbol{r}}(\boldsymbol{k}) = h^{\widetilde{\alpha\sigma},\widetilde{\beta'\sigma'}}_{\boldsymbol{r}}(C_3\boldsymbol{k}) \tag{B27}$$

is satisfied and Eq. (B14) is satisfied by using Eq. (B20).

(iii) Time-reversal symmetry. The time-reversed Hamiltonian is

$$\mathcal{T}H\mathcal{T}^\dagger = \sum_{\boldsymbol{r}_j} \sum_{\alpha\sigma,\beta'\sigma'} \sum_{pq} t^{\alpha\sigma,\beta'\sigma'\,*}_{pq}(\boldsymbol{r}_i)\, c^\dagger_{\alpha\bar{\sigma}}[\boldsymbol{r}_j + \boldsymbol{d}_\alpha(\boldsymbol{r}_j)] c_{\beta'\bar{\sigma}'}[\boldsymbol{r}_j + \boldsymbol{d}_{\beta'}(\boldsymbol{r}_j) + \boldsymbol{a}_{pq}](-1)^{1-\delta_{\sigma\sigma'}}$$

$$= \int d\boldsymbol{k}\, d\boldsymbol{k}' \sum_{\boldsymbol{r}_j} \sum_{\alpha\sigma,\beta'\sigma'} \left[\sum_{pq} t^{\alpha\sigma,\beta'\sigma'}_{pq}(\boldsymbol{r}_j) e^{i\boldsymbol{k}\cdot\boldsymbol{d}_\alpha(\boldsymbol{r}_j)} e^{i\boldsymbol{k}'\cdot(\boldsymbol{d}_{\beta'}(\boldsymbol{r}_j)+\boldsymbol{a}_{pq})} \right]^* e^{i(-\boldsymbol{k}+\boldsymbol{k}')\cdot\boldsymbol{r}_j} \, c^\dagger_{\alpha\bar{\sigma},\boldsymbol{k}} c_{\beta'\bar{\sigma}',\boldsymbol{k}'}(-1)^{1-\delta_{\sigma\sigma'}}$$

$$= \int d\boldsymbol{k}\, d\boldsymbol{k}' \sum_{\boldsymbol{r}_j} \sum_{\alpha\sigma,\beta'\sigma'} \sum_{\boldsymbol{G}_l} e^{-i\boldsymbol{G}_l\cdot\boldsymbol{r}_j} \, t^{\alpha\sigma,\beta'\sigma'}_{-\boldsymbol{k},-\boldsymbol{k}',\boldsymbol{G}_l}{}^* e^{i(-\boldsymbol{k}+\boldsymbol{k}')\cdot\boldsymbol{r}_j} \, c^\dagger_{\alpha\bar{\sigma},\boldsymbol{k}} c_{\beta'\bar{\sigma}',\boldsymbol{k}'}(-1)^{1-\delta_{\sigma\sigma'}}$$

$$= \int d\boldsymbol{k} \sum_{\alpha\sigma,\beta'\sigma'} \sum_{\boldsymbol{G}_l} t^{\alpha\sigma,\beta'\sigma'}_{-\boldsymbol{k},-\boldsymbol{k}-\boldsymbol{G}_l,\boldsymbol{G}_l}{}^* \, c^\dagger_{\alpha\bar{\sigma},\boldsymbol{k}} c_{\beta'\bar{\sigma}',\boldsymbol{k}+\boldsymbol{G}_l}(-1)^{1-\delta_{\sigma\sigma'}}, \tag{B28}$$

where $\bar{\sigma}$ means the opposite spin. The conditions for this to be time-reversal symmetric [Eq. (B15)] are

$$(-1)^{1-\delta_{\sigma\sigma'}} \, t^{\alpha\sigma,\beta'\sigma'}_{-\boldsymbol{k},-\boldsymbol{k}-\boldsymbol{G}_l,\boldsymbol{G}_l}{}^* = t^{\alpha\bar{\sigma},\beta'\bar{\sigma}'}_{\boldsymbol{k},\boldsymbol{k}+\boldsymbol{G}_l,-\boldsymbol{G}_l}. \tag{B29}$$

When the Hamiltonian of the untwisted structures is time-reversal symmetric,

$$h^{\alpha\sigma,\beta'\sigma'}_{\boldsymbol{r}}(\boldsymbol{k})^* = (-1)^{1-\delta_{\sigma\sigma'}} \, h^{\alpha\bar{\sigma},\beta'\bar{\sigma}'}_{\boldsymbol{r}}(-\boldsymbol{k}) \tag{B30}$$

is satisfied and Eq. (B15) is satisfied by using Eq. (B20).

APPENDIX C: NUMERICAL CALCULATION METHODS

In this Appendix, we describe methods used in our numerical calculations.

1. Matrix representation

We have obtained the Hamiltonian of the moiré system,

$$H = \int d\boldsymbol{k} \sum_{\alpha\sigma,\beta'\sigma'} \sum_{\boldsymbol{G}_l} t^{\alpha\sigma,\beta'\sigma'}_{\boldsymbol{k},\boldsymbol{k}-\boldsymbol{G}_l,\boldsymbol{G}_l} \, c^\dagger_{\alpha\sigma,\boldsymbol{k}} c_{\beta'\sigma',\boldsymbol{k}-\boldsymbol{G}_l}, \tag{C1}$$

and here we give the matrix representation of this Hamiltonian so that it can be implemented in numerical calculations.

Because all hopping processes have momentum difference $\boldsymbol{G}_l$, the basis is given for $\boldsymbol{k} \in$ moiré BZ as

$$\{c_{\alpha\sigma,\boldsymbol{k}+\boldsymbol{v}_{mn}} | \boldsymbol{v}_{mn} = m\boldsymbol{G}_1 + n\boldsymbol{G}_2, \; m,n \in \mathbb{Z}\}. \tag{C2}$$

To describe low-energy physics with a finite-dimension matrix, we take a momentum cutoff k_c as an approximation. In the Bi_2Te_3 system, the low-energy physics is described around the Γ point. Therefore, we take a finite basis as

$$\{c_{\alpha\sigma,\boldsymbol{k}+\boldsymbol{v}_{mn}} | \boldsymbol{v}_{mn} = m\boldsymbol{G}_1 + n\boldsymbol{G}_2, \; m,n \in \mathbb{Z}, |\boldsymbol{v}_{mn}| < k_c\}. \tag{C3}$$

With this basis, the matrix representation of the Hamiltonian is

$$H(\boldsymbol{k}) = \begin{pmatrix} t_{\boldsymbol{k},\boldsymbol{k},\boldsymbol{0}} & & & & \text{if } \boldsymbol{v}_{mn} - \boldsymbol{v}_{m'n'} = \boldsymbol{G}_l \\ & \ddots & & & \downarrow \\ & & t_{\boldsymbol{k}+\boldsymbol{v}_{mn},\boldsymbol{k}+\boldsymbol{v}_{mn},\boldsymbol{0}} & \cdots & t_{\boldsymbol{k}+\boldsymbol{v}_{mn},\boldsymbol{k}+\boldsymbol{v}_{m'n'},\boldsymbol{G}_l} \\ & & & \ddots & \vdots \\ & & & & t_{\boldsymbol{k}+\boldsymbol{v}_{m'n'},\boldsymbol{k}+\boldsymbol{v}_{m'n'},\boldsymbol{0}} \\ & & & & & \ddots \end{pmatrix}, \tag{C4}$$

where $\boldsymbol{k} \in$ moiré BZ.

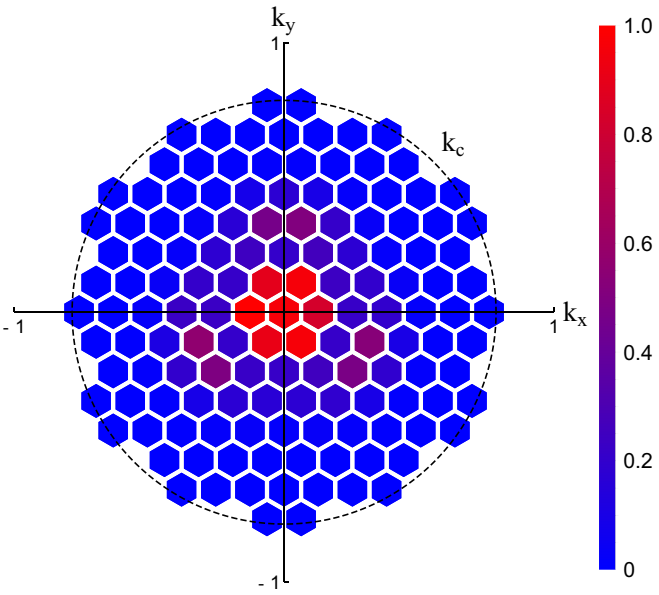

FIG. 12. Weight mapping of the 17th valence band at the Γ point of twisted bilayer $Bi_2(Te_{0.92}Se_{0.08})_3$ with a twist angle $\theta = 1.0^\circ$ and cutoff $k_c = \pi/4$. The hexagons are moiré BZs and their colors represent the weight on them (normalized with the maximum value). In this case, it can be seen that the cutoff is large enough.

Because we consider only seven $\boldsymbol{G}_l$, an off-diagonal block is nonzero only when $\boldsymbol{v}_{mn} - \boldsymbol{v}_{m'n'}$ matches one of the seven $\boldsymbol{G}_l$.

2. Validity of the cutoff k_c

The validity of the cutoff k_c is evaluated as follows. Once we calculate a wave function $\psi_{\boldsymbol{k}}$, and make a weight mapping onto moiré BZs within k_c as

$$\psi_{\boldsymbol{k}} = \begin{pmatrix} \phi_1 \\ \phi_2 \\ \vdots \end{pmatrix} \mapsto \begin{pmatrix} \sum_{l=1}^{60} |\phi_l|^2 \\ \sum_{l=61}^{120} |\phi_l|^2 \\ \vdots \end{pmatrix} \begin{matrix} \leftarrow \text{weight on moiré BZ\#1} \\ \leftarrow \text{weight on moiré BZ\#2} \\ \vdots \end{matrix}. \tag{C5}$$

By plotting the weight mapping, we check the weight on the BZs around k_c. If the BZs around k_c have small weights, the cutoff k_c is large enough and the effect of k_c is negligible. If the BZs around k_c have significant weight compared to other BZs, larger k_c should be taken. Generally, wave functions whose energies are far from Fermi level require larger k_c. Therefore, evaluating with wave functions that are distant from the Fermi level ensures the validity of k_c for wave functions that are closer to the Fermi level. Figure 12 is an example of the weight mapping for the 17th valence band of $Bi_2(Te_{0.92}Se_{0.08})_3$ with a twist angle $\theta = 1.0^\circ$, cutoff $k_c = \pi/4$. Each hexagon represents a moiré BZ, and its color represents the weight (normalized with the maximum value). It can be seen that the moiré BZs around k_c have almost no weights and thus the cutoff is large enough at least for the 1st $\sim$ 17th valence bands in this case. The validity of k_c has been confirmed in all calculations in this paper.

3. Periodicity in the momentum space

From the Bloch theorem, a wave function $\psi_{\boldsymbol{k}+\boldsymbol{G}_l}$ is physically identical with $\psi_{\boldsymbol{k}}$, and thus $|\langle\psi_{\boldsymbol{k}+\boldsymbol{G}_l}|\psi_{\boldsymbol{k}}\rangle| = 1$. This fact is used in the numerical evaluation of the Wilson loop spectra.

In the effective model of a moiré superlattice system with basis (C3), the momentum shift $\boldsymbol{k} \to \boldsymbol{k} + \boldsymbol{G}_l$ effectively results in a shift in $\boldsymbol{v}_{mn}$ indices. Therefore, components of a numerically obtained eigenvector $\psi_{\boldsymbol{k}+\boldsymbol{G}_l}$ are shifted from those of $\psi_{\boldsymbol{k}}$, and $|\langle\psi_{\boldsymbol{k}+\boldsymbol{G}_l}|\psi_{\boldsymbol{k}}\rangle| \neq 1$ due to the $\boldsymbol{k}$ dependence of the basis. Note that, as long as the cutoff k_c is large enough, i.e., no significant component is put outside of the cutoff by the shift, $\psi_{\boldsymbol{k}+\boldsymbol{G}_l}$ and $\psi_{\boldsymbol{k}}$ are physically identical states. To evaluate the inner product of wave functions $\psi_{\boldsymbol{k}+\boldsymbol{G}_l}$ and $\psi_{\boldsymbol{k}}$ correctly with the numerically obtained eigenvectors, we introduce a basis-shift matrix T, which is defined as

$$T = \{T_{(mn)(m'n')}\} = \begin{cases} I_\eta, & \boldsymbol{v}_{mn} + \boldsymbol{G}_l = \boldsymbol{v}_{m'n'} \\ O_\eta, & \text{others} \end{cases} \tag{C6}$$

where η is the orbital-spin degree of freedom [$\eta = 60$ in twisted bilayer $Bi_2(Te_{1-x}Se_x)_3$], and I_η and O_η are the η-dimension identity matrix and zero matrix, respectively. By using this T, the inner product of wave functions $\psi_{\boldsymbol{k}+\boldsymbol{G}_l}$ and $\psi_{\boldsymbol{k}}$ is evaluated as $\langle\psi_{\boldsymbol{k}+\boldsymbol{G}_l}|T|\psi_{\boldsymbol{k}}\rangle$, which approximately satisfies $|\langle\psi_{\boldsymbol{k}+\boldsymbol{G}_l}|T|\psi_{\boldsymbol{k}}\rangle| = 1$ when the cutoff is large enough.

4. Wannierization and surface-state calculation

To calculate surface states, we construct Wannier functions from wave functions and a band dispersion obtained from the effective model. We use the option `use_bloch_phases=T` of the WANNIER90 [50] to set the Bloch functions as the initial guess for the projections. In calculations with this option, we need a list of eigenenergies $E_{n\boldsymbol{k}}$ in file `prefix.eig` and a list of wave-function overlaps $\langle\psi_{\boldsymbol{k}+\delta\boldsymbol{k}}|\psi_{\boldsymbol{k}}\rangle$ in file `prefix.mmn` for the target bands. These lists are numerically obtained from the effective model calculation. Both of them should be calculated with $\boldsymbol{k}$ mesh taken over the moiré BZ. Note that in the calculation of overlaps, the basis-shift matrix given in Appendix C 3 should be used for overlaps across the boundary of the moiré BZ. With this method, Wannier functions and hoppings between them are obtained for moiré bands. With the obtained parameters, edge-state spectra are calculated by the Green's function method implemented in the WANNIERTOOLSpackage [54].

For the parameters obtained by the Wannierization, we make a correction to recover the time-reversal symmetry. It is because the energy scale of a moiré superlattice system is so small that numerical errors in the first-principles calculations in untwisted systems get more noticeable. The correction is done by replacing the hopping parameters as

$$t^{\alpha\sigma,\beta'\sigma'}_{\boldsymbol{a}_{nm}} \to \tfrac{1}{2}\left(t^{\alpha\sigma,\beta'\sigma'}_{\boldsymbol{a}_{nm}} + (-1)^{1-\delta_{\sigma\sigma'}} t^{\alpha\bar{\sigma},\beta'\bar{\sigma}'\,*}_{\boldsymbol{a}_{nm}}\right), \tag{C7}$$

where $\bar{\sigma}$ is the opposite spin of σ. The $\delta_{\sigma\sigma'}$ is the Kronecker delta for spin σ and σ', which essentially comes from $\mathcal{T}^2 = -1$ in a spin-$\frac{1}{2}$ system. We have confirmed that this correction works only as a minor correction in the edge-state spectra.

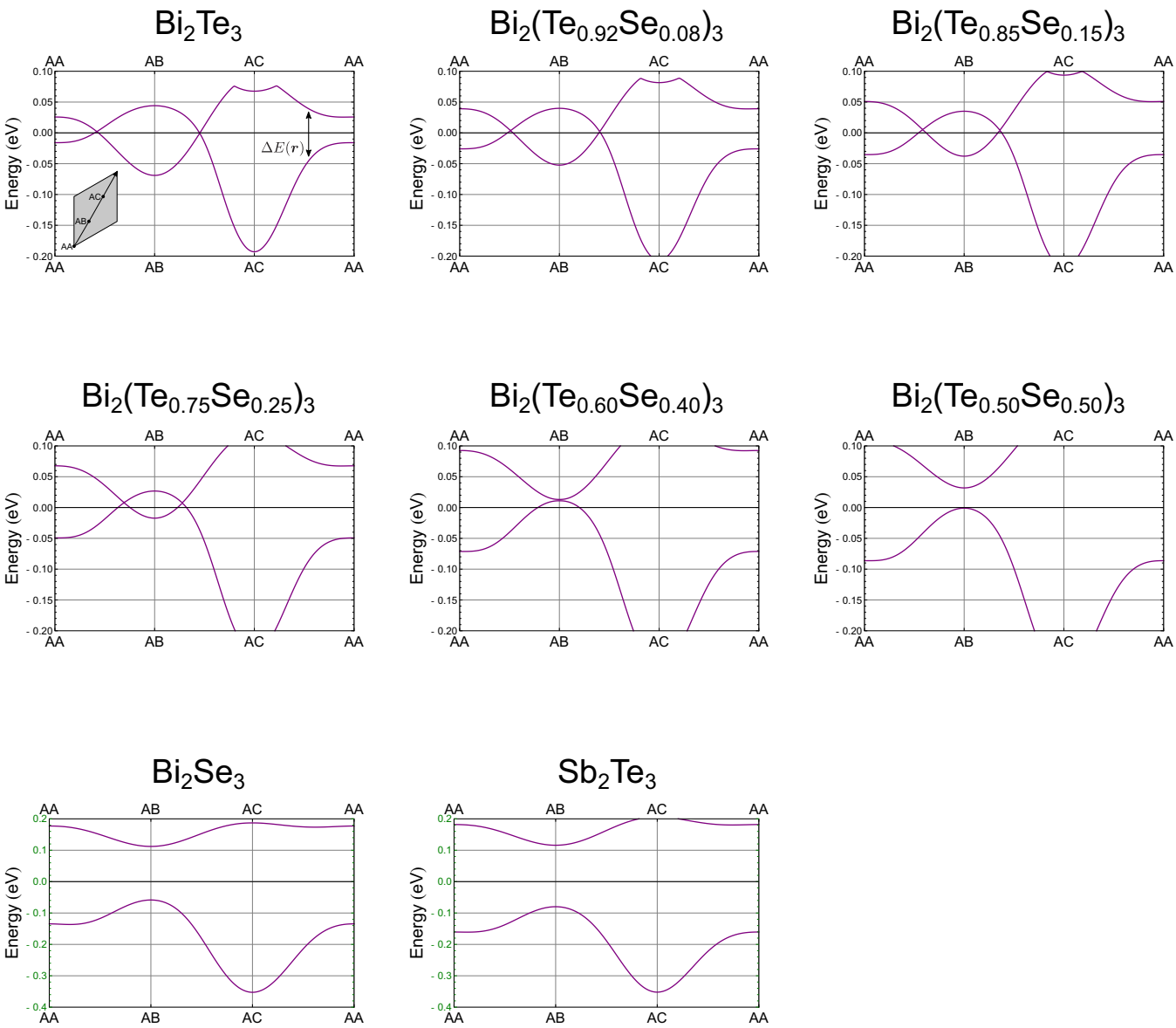

FIG. 13. Energies of the valence top band and the conduction bottom band at the Γ point plotted along the (AA-AB-AC-AA)-stacking line for Bi_2Te_3, $Bi_2(Te_{1-x}Se_x)_3$ with various x, Bi_2Se_3, and Sb_2Te_3. Note that the Bi_2Se_3 and Sb_2Te_3 cases are plotted in a different energy range.

5. Symmetry in wave-function plot

Twisted bilayer $Bi_2(Te_{1-x}Se_x)_3$ has the time-reversal symmetry and the layer group symmetry No. 67, which include C_{3z}-rotation symmetry. Due to the time-reversal symmetry, all bands at the Γ point appear as doubly degenerate Kramers pairs. Because the numerical diagonalization does not necessarily give simultaneous eigenvectors of the Hamiltonian and the C_{3z} rotation, we need to symmetrize the Kramers pair to obtain a C_{3z}-symmetric wave-function plot at the Γ point.

For a given Kramers pair $|\psi_1\rangle, |\psi_2\rangle$ and C_{3z} operator, a matrix representation of $\Gamma_{C_{3z}}$ is given as

$$\Gamma_{C_{3z}} = \begin{pmatrix} \langle\psi_1|C_{3z}|\psi_1\rangle & \langle\psi_1|C_{3z}|\psi_2\rangle \\ \langle\psi_2|C_{3z}|\psi_1\rangle & \langle\psi_2|C_{3z}|\psi_2\rangle \end{pmatrix}. \tag{C8}$$

With a unitary transform U that diagonalizes $\Gamma_{C_{3z}}$ as $U^\dagger \Gamma_{C_{3z}} U = \mathrm{diag}(\lambda_1, \lambda_2)$, symmetrized wave functions $|\tilde{\psi}_1\rangle, |\tilde{\psi}_2\rangle$ are obtained as

$$(|\tilde{\psi}_1\rangle \quad |\tilde{\psi}_2\rangle) = (|\psi_1\rangle \quad |\psi_2\rangle)U. \tag{C9}$$

APPENDIX D: EFFECT OF SE DOPING ON TWISTED BILAYER $Bi_2(Te_{1-x}Se_x)_3$

In this section, we discuss the effect of Se doping in in twisted bilayer $Bi_2(Te_{1-x}Se_x)_3$. First, we see the Se-doping effect in parameters of untwisted $Bi_2(Te_{1-x}Se_x)_3$ systems. Next, we see the moiré band dispersions for various Se-doping values.

1. Effect of Se doping on parameters in untwisted bilayer $Bi_2(Te_{1-x}Se_x)_3$

The discrete Fourier transform (B16) interpolates the untwisted Hamiltonians to the intermediate area. Therefore, we

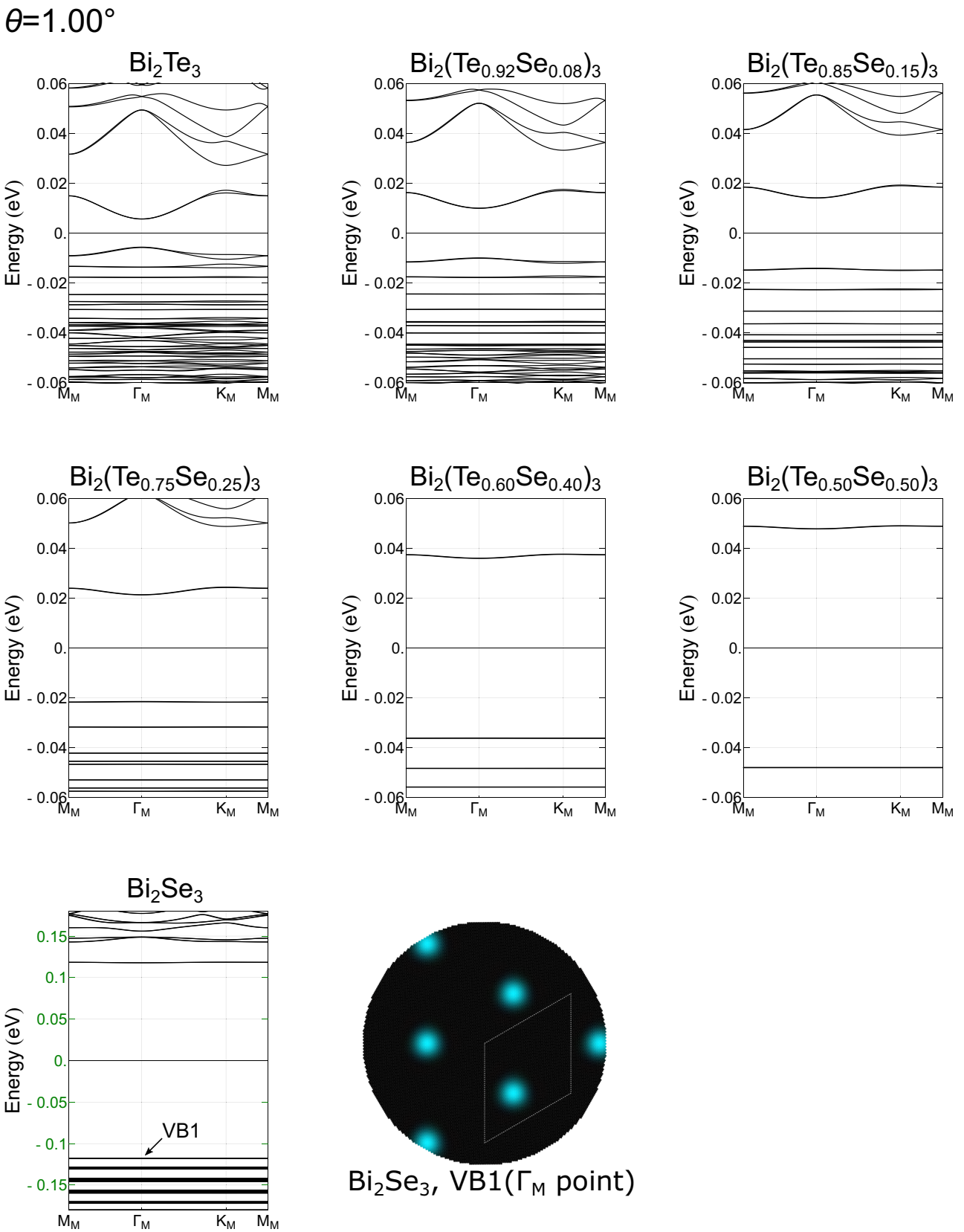

FIG. 14. Moiré band dispersions of twisted bilayer $Bi_2(Te_{1-x}Se_x)_3$ for various x. The twist angle is fixed at $\theta = 1.00^\circ$. Note that the Bi_2Se_3 case is plotted in a different energy range. A wave function of the valence top band at the Γ_M point (upper layer, lower Bi atom, p_z orbital, spin-up component) is also shown.

can define 'band gap in each real-space position $\boldsymbol{r}$" in the moiré unit cell, and it can be used to estimate where the topological domain boundary is. To evaluate the band gap in the Γ point in the small twist angle limit, we consider $\boldsymbol{k} = \boldsymbol{0}$ in Eq. (B16) as

$$\sum_{\boldsymbol{G}_l} e^{i\boldsymbol{G}_l\cdot\boldsymbol{r}}\, t^{\alpha\sigma,\beta'\sigma'}_{\boldsymbol{0},-\boldsymbol{G}_l,\boldsymbol{G}_l} = h^{\alpha\sigma,\beta'\sigma'}_{\boldsymbol{r}}(\boldsymbol{0}), \tag{D1}$$

where $t^{\alpha\sigma,\beta'\sigma'}_{\boldsymbol{0},-\boldsymbol{G}_l,\boldsymbol{G}_l}$ are given in Eq. (B20). Note that $\boldsymbol{G}_l$ are negligible compared to the atomic BZ in the small twist angle limit. By diagonalizing the right-hand side, we obtain a band gap $\Delta E(\boldsymbol{r})$. The position where $\Delta E(\boldsymbol{r}) = 0$ is satisfied is the topological domain boundary. In Fig. 13, the energies of the valence top band and the conduction bottom band at the Γ point calculated with Eq. (D1) are plotted along the (AA-AB-AC-AA)-stacking line for Bi_2Te_3, $Bi_2(Te_{1-x}Se_x)_3$ with various x, Bi_2Se_3, and Sb_2Te_3. Here, we calculate the electronic band structure of Sb_2Te_3 under the same condition as Bi_2Te_3 and Bi_2Se_3. Note that Bi_2Se_3 and Sb_2Te_3 cases are plotted in a different energy range. $\Delta E(\boldsymbol{r}) = 0$ is the gap between the two bands in $\boldsymbol{r}$ (horizontal axis).

As shown in the main paper, the valence and conduction bands in Bi_2Te_3 are inverted only around the AB-stacking case. As Se is doped (x gets larger), the (inverted) band gap in the AB-stacking area gets smaller, and the band gap in the AA- and AC-stacking area get larger. Around $Bi_2(Te_{0.60}Se_{0.40})_3$ ($x = 0.40$), a band touching occurs at the AB-stacking point, and the band structure in the AB-stacking area becomes trivial in the $x > 0.40$ region. Because the plots of Bi_2Se_3 and Sb_2Te_3 are almost identical, it can be seen that replacing Bi with Sb has a similar effect as replacing Te with Se.

2. Effect of Se doping on moiré band dispersion

Figure 14 shows moiré band dispersions of twisted bilayer $Bi_2(Te_{1-x}Se_x)_3$ for various x. The twist angle is fixed at $\theta = 1.00°$. The values of x are the same as those in Fig. 13. After the gap closing at the AB stacking occurs ($x > 0.40$), the edge-state-originated bands disappear and the band gap around the Fermi level gets larger. For twisted bilayer Bi_2Se_3, a wave function of the valence top band at the Γ_M point is plotted. The wave function is found to be a bulk-originated state around the AB-stacking area.

APPENDIX E: SUPPLEMENTAL INFORMATION OF TWISTED BILAYER $Bi_2(Te_{1-x}Se_x)_3$

In this Appendix, we give supplemental information of twisted bilayer $Bi_2(Te_{1-x}Se_x)_3$.

1. Angular momentum of edge-state-originated bands

When a wave function is plotted for an edge-state-originated band, it appears to have an integer angular momentum. However, the electronic state is coupled with spin degree of freedom and thus the total angular momentum is a half-integer. Actually, when both of spin-up and spin-down components are plotted for a wave function, the phase winding number (≈orbital angular momentum) is different by 1 (Fig. 15). By coupling the orbital and spin angular momentum, a total angular momentum (or a rotation eigenvalue of the wave function) is uniquely defined.

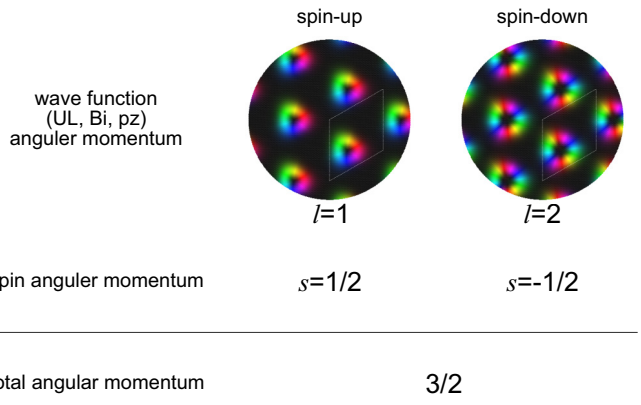

FIG. 15. Example of the wave function and angular momentum in the VB2 of twisted bilayer $Bi_2(Te_{0.85}Se_{0.15})_3$ with $\theta = 0.50°$. The wave function plots show the components of spin up and spin down on (upper layer, lower Bi atom, p_z orbital). The total angular momentum of this wave function is calculated as $\frac{3}{2}$.

2. Twist angle dependence of the bandwidth

Figure 16 shows the twist angle dependence of the bandwidth of VB1-4 in twisted bilayer $Bi_2(Te_{0.85}Se_{0.15})_3$. The bandwidth is estimated as $\mathrm{Max}[E(\boldsymbol{k})] - \mathrm{Min}[E(\boldsymbol{k})]$ ($\boldsymbol{k} \in \{M_M\text{-}\Gamma_M\text{-}K_M\text{-}M_M$ line$\}$). As a general trend, the bandwidth tends to increase as the twist angle increases. This tendency is explained by the band folding in the moiré BZ, as explained in the main text. More detailed behavior is determined by a combination of multiple factors such as Rashba splitting and hybridization with other bands.

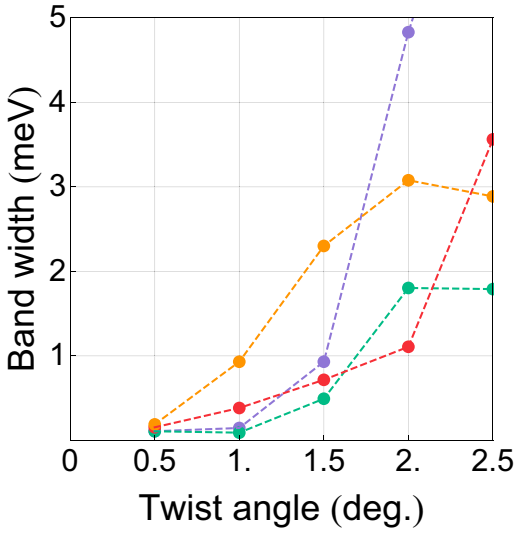

FIG. 16. Twist angle dependence of the bandwidth of VB1 (orange), VB2 (red), VB3 (green), and VB4 (purple) in twisted bilayer $Bi_2(Te_{0.85}Se_{0.15})_3$. The bandwidth is estimated with the band dispersion along the M_M-Γ_M-K_M-M_M line.

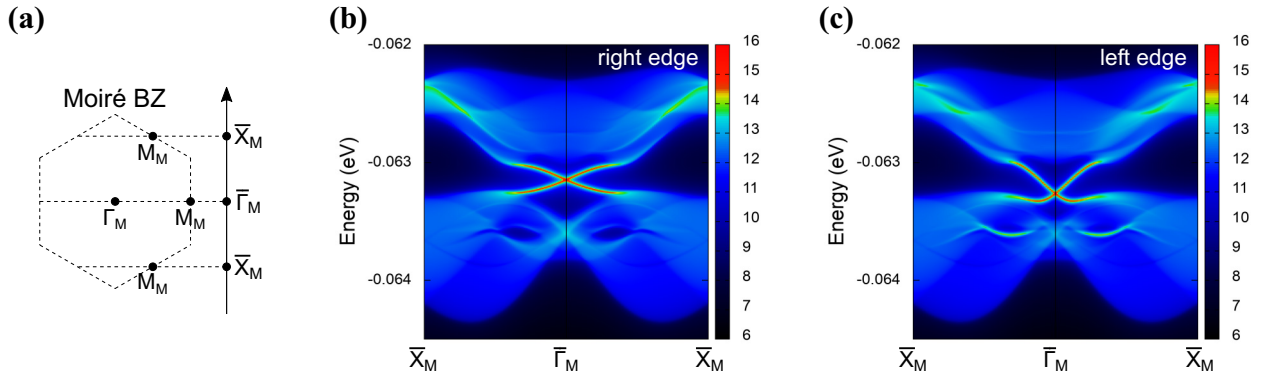

FIG. 17. Edge dependence of edge-state spectra. (a) The edge BZ used in the edge-state calculations. (b), (c) Edge-state spectra of the right edge and left edge in twisted bilayer $Bi_2(Te_{0.92}Se_{0.08})_3$.

3. Edge dependence of moiré edge-state spectra

Here, we compare the edge-state spectra for the left and right edges. Note that the left and right edges are defined by using the moiré unit cell as a unit to build the half-infinite plane, i.e., the left edge (right edge) of the moiré unit cell appears on the left edge (right edge) of the half-infinite plane. Figure 17 shows the edge BZ (a) and edge-state spectra of the right edge (b) and left edge (c) in twisted bilayer $Bi_2(Te_{0.92}Se_{0.08})_3$. The edge-state spectra are topologically identical for both edges, but the energies of the Dirac cones of the edge states are different. It is because there is no symmetry to guarantee the equivalence of their energies in twisted bilayer $Bi_2(Te_{0.92}Se_{0.08})_3$. Although the moiré superlattice of twisted bilayer $Bi_2(Te_{1-x}Se_x)_3$ has in-plane C_2-rotation symmetries along the Γ_M-M_M lines, they do not exchange the two edges. Therefore, each edge state does not necessarily have the same spectrum. This edge dependence is not moiré specific but generally found in a noncentrosymmetric 2D topological insulator. See Appendix F for general and more detailed discussion. Note that in more realistic conditions, the energy difference between the two edge states may be suppressed by the charge-neutral condition.

4. Topological phase transition in moiré bands

Here, we show how a gap closing and a topological phase transition occur in moiré bands. As the twist angle get smaller, more edge-state-originated nearly flat bands appear around the Fermi level due to the band folding with the small moiré BZ. For example, in the case of twisted bilayer $Bi_2(Te_{0.92}Se_{0.08})_3$ with $\theta \sim 1.55^\circ$, topological phase transitions occur on VB8 and VB9 and eventually they become topologically trivial bands as the twist angle is decreased. Generally for the topological phase transition in twisted bilayer $Bi_2(Te_{1-x}Se_x)_3$, the gap closing occurs on the Γ_M-K_M lines due to the in-plane C_2 rotation symmetry [70]. Note that the Γ_M-K_M lines are not high-symmetry lines, although the position of the gap closing is determined by the symmetry restriction. When edges are made so that there is no symmetry between the two edges, the gap closing is also seen in the 1D edge BZ as a gap closing of bulk-band spectra at general momenta. Figure 18 shows a bulk-band spectra and an edge-band spectra of twisted bilayer $Bi_2(Te_{0.92}Se_{0.08})_3$ with the twist angle $\theta = 1.35^\circ$, which is close to a phase transition point. Gap-closing points are indicated with white dashed circles. Note that the edge states appear from the points where the gap closing will occur and make a Dirac cone that is close to the

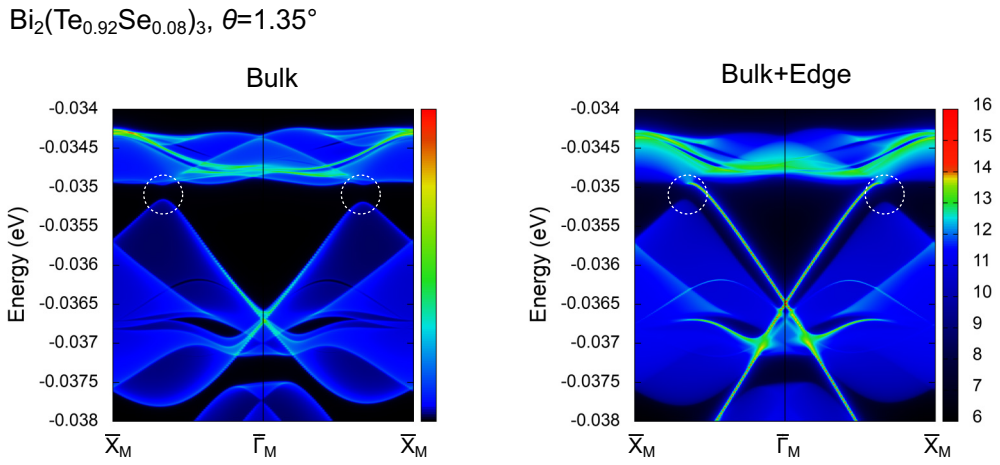

FIG. 18. Bulk and edge band spectra of twisted bilayer $Bi_2(Te_{0.92}Se_{0.08})_3$ with $\theta = 1.35^\circ$. The gap closing of the bulk band spectra occurs at general momenta (white dashed circles).

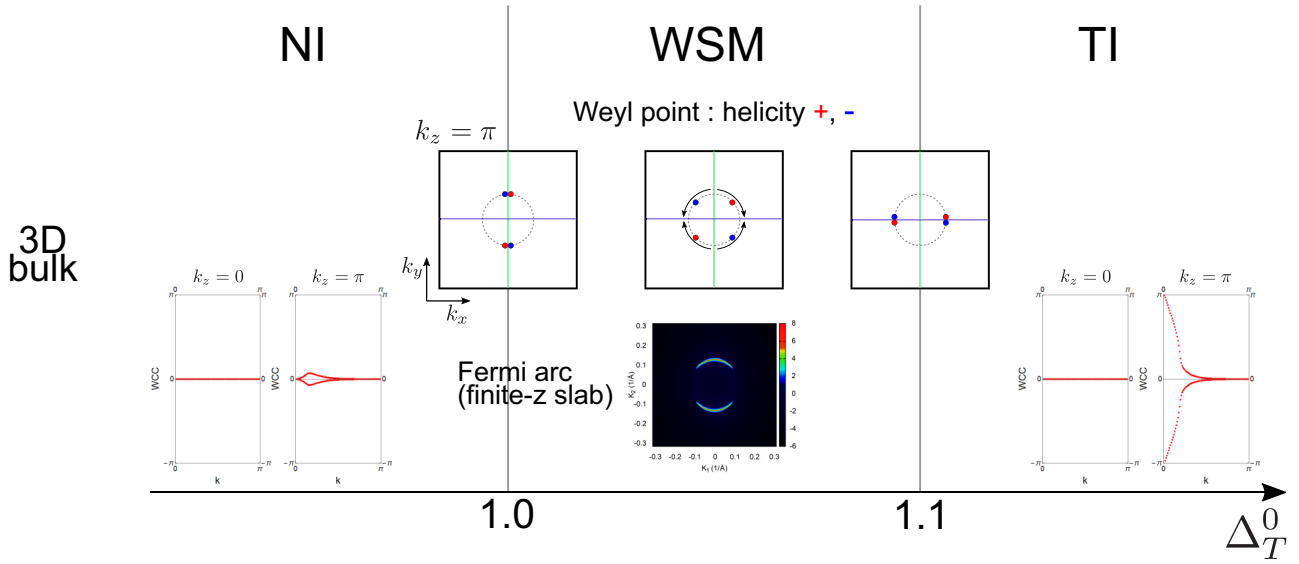

FIG. 19. Phase diagram of 3D WSM model (F3). A WSM phase appears between $\Delta_T^0 = 1.0$ and 1.1 as a gapless phase between NI and TI. At $\Delta_T^0 = 1.0$, Weyl points are created on the $(k_x = 0, k_z = \pi)$ line. As Δ_T^0 increases, the Weyl points move in the $k_z = \pi$ plane and annihilate on the $(k_y = 0, k_z = \pi)$ line at $\Delta_T^0 = 1.1$.

bulk-band crossing of a Kramers pair at the $\bar{\Gamma}_M$ point. The topological phase transition that occurs as the twist angle is decreased is not simple as a pair annihilation between VB8 and VB9. As the twist angle is decreased, the gap between edge-state-originated bands gets smaller and thus they shift relatively upward, while the bulk-state-originated band stays. Therefore, the nontrivial structure moves to the next and next band as the twist angle is decreased. Actually, another gap closing occurs between VB9 and VB10 and there are midgap edge states in the lower-energy region VB9 in Fig. 18.

APPENDIX F: NONCENTROSYMMETRIC 2D TOPOLOGICAL PHASE TRANSITION

A moiré system does not have the inversion symmetry and we have found that a topological phase transition occurs in twisted $Bi_2(Te_{1-x}Se_x)_3$. In this Appendix, we explain how a topological phase transition occurs in a general noncentrosymmetric 2D system. We consider a topological phase transition between a topological insulator (TI) phase and a normal insulator (NI) phase in time-reversal $\mathcal{T}$ symmetric systems. Generally, when a topological phase transition occurs, a gap closing must occur in the bulk-band dispersion [55,56]. First, we briefly review the case of a centrosymmetric TI. In a phase transition occurs from a NI to a TI in a centrosymmetric system, the bulk gap closing occurs at one of (or an odd number of) the TRIM. When a surface band spectrum is drawn, the gap closing is seen as a gap closing of the bulk continuous spectra at one of the TRIM of the surface BZ because TRIM of 3D BZ are projected on TRIM of the surface BZ. In the TI phase, a corresponding surface state emerges around the TRIM in which the gap closing occurred. In noncentrosymmetric systems, the bulk gap closing occurs at a generic $\boldsymbol{k}$ point. In 3D case, the gapless phase has finite width in the parameter space, which is a Weyl semimetal (WSM) phase. In the 2D case, the gap closing occurs only on the critical point in the parameter space. Because the bulk gap closing occurs at a generic $\boldsymbol{k}$ point, a gap closing in the surface band spectrum should also be seen at a generic $\boldsymbol{k}$ in the surface BZ. Reference [70] clarified that, in noncentrosymmetric 2D systems, $\boldsymbol{k}$ points where the gap closing can occur are restricted by crystalline symmetries. However, it has not been clearly described how a corresponding surface state emerges from the gap-closing point in the surface band spectrum. Therefore, here we demonstrate the emergence of the surface state in topological phase transition in noncentrosymmetric 2D systems, and explain the relation between the surface state and the crystalline symmetries.

As explained above, in a 3D system, a topological phase transition in a noncentrosymmetric system is described as a NI-WSM-TI transition. Therefore, we start from a 3D model that describes a NI-WSM-TI transition, and by focusing a particular 2D momentum plane in the model we discuss the bulk and surface band spectra in a noncentrosymmetric 2D system. We use the inversion-broken TI/NI multilayer model given in Refs. [71,72], and it is a 4×4 model written as

$$H = v\tau_z(k_y\sigma_x - k_x\sigma_y) + V\tau_z + \Delta_N(\boldsymbol{k})\tau_x + \Delta_T(\boldsymbol{k})(e^{ik_z}\tau_+ + e^{-ik_z}\tau_-). \quad \text{(F1)}$$

The four components consist of surface states on the top surface of the TI layer with spin up and down $(t_{\uparrow\boldsymbol{k}}, t_{\downarrow\boldsymbol{k}})$, and those on the bottom surface $(b_{\uparrow\boldsymbol{k}}, b_{\downarrow\boldsymbol{k}})$. The $\sigma_{x,y,z}$ and $\tau_{x,y,z}$ are Pauli matrices for spin and top and bottom surfaces, respectively, where $\tau_\pm = (\tau_x \pm i\tau_y)/\sqrt{2}$. We assume a twofold rotation symmetry about the z axis (C_{2z}), and thus the $\Delta_N(\boldsymbol{k})$ and $\Delta_T(\boldsymbol{k})$ are written as

$$\Delta_T(\boldsymbol{k}) = \Delta_T^0 + \delta_T^x k_x^2 + \delta_T^y k_y^2,$$
$$\Delta_N(\boldsymbol{k}) = \Delta_N^0 + \delta_N^x k_x^2 + \delta_N^y k_y^2. \quad \text{(F2)}$$

To draw the surface band spectrum, we transform the model into an equivalent lattice periodic model. The lattice

periodic model is

$$H = v\tau_z(\sin k_y\sigma_x - \sin k_x\sigma_y) + V\tau_z + \Delta_T(\boldsymbol{k})\tau_x + \Delta_N(\boldsymbol{k})(e^{ik_z}\tau_+ + e^{-ik_z}\tau_-), \quad \text{(F3)}$$

where $\Delta_N(\boldsymbol{k})$ and $\Delta_T(\boldsymbol{k})$ are written as

$$\Delta_T(\boldsymbol{k}) = \Delta_T^0 + 2\delta_T^x(1-\cos k_x) + 2\delta_T^y(1-\cos k_y),$$
$$\Delta_N(\boldsymbol{k}) = \Delta_N^0 + 2\delta_N^x(1-\cos k_x) + 2\delta_N^y(1-\cos k_y). \quad \text{(F4)}$$

By taking Δ_T^0 as a tuning parameter, this model shows the NI-WSM-TI transition. We fix the other parameters as

$$V = 0.2, \quad v = 0.4, \quad \delta_N^x = 0.60, \quad \delta_T^x = 0.20,$$
$$\delta_N^y = \delta_N^x\left(1 + \frac{0.1}{\delta_T^x - \delta_N^x}\frac{1/2}{1-\sqrt{1-V^2/v^2}}\right),$$
$$\delta_T^y = \delta_T^x\left(1 + \frac{0.1}{\delta_T^x - \delta_N^x}\frac{1/2}{1-\sqrt{1-V^2/v^2}}\right),$$
$$\Delta_N^0 = 1.0 + 2\left(\delta_T^y - \delta_N^y\right)\left(1-\sqrt{1-V^2/v^2}\right). \quad \text{(F5)}$$

Here, δ_N^y, δ_T^y, and Δ_N^0 are determined to fix the transition points at $\Delta_T^0 = 1.0$ and 1.1. When $\Delta_T^0 < 1.0$, the model is a normal insulator (Fig. 19). When $\Delta_T^0 = 1.0$, Weyl points are created as pairs on the $(k_z = \pi,\ k_x = 0)$ line (Fig. 19). Due to the time-reversal symmetry, a pair of Weyl points are created each of positive and negative k_y region and thus four Weyl points are created in total. When $1.0 < \Delta_T^0 < 1.1$, the Weyl points move on the $k_z = \pi$ plane, and when $\Delta_T^0 = 1.1$, they annihilate on the $(k_z = \pi,\ k_y = 0)$ line. When $\Delta_T^0 > 1.1$, the model is a strong topological insulator.

By focusing on a particular 2D momentum space in the 3D BZ of this model, we can discuss a topological phase transition and surface states in a noncentrosymmetric 2D system. To consider a time-reversal symmetric system, the focused 2D plane must be a time-reversal invariant plane ($\forall\, \boldsymbol{k} \in \{\text{2D plane}\}, -\boldsymbol{k} \in \{\text{2D plane}\}$). Here we focus on two planes, $k_x = 0$ and $k_y = 0$. To draw the surface band spectrum with Green's function method, we transform the lattice periodic model into a real space representation as

$$\begin{aligned} H = \sum_{\boldsymbol{r}} \Big[& i\frac{v}{2}(-t_{\uparrow\boldsymbol{r}}^\dagger t_{\downarrow\boldsymbol{r}+y} + t_{\uparrow\boldsymbol{r}}^\dagger t_{\downarrow\boldsymbol{r}-y} + b_{\uparrow\boldsymbol{r}}^\dagger b_{\downarrow\boldsymbol{r}+y} - b_{\uparrow\boldsymbol{r}}^\dagger b_{\downarrow\boldsymbol{r}-y}) + \frac{v}{2}(t_{\uparrow\boldsymbol{r}}^\dagger t_{\downarrow\boldsymbol{r}+x} - t_{\uparrow\boldsymbol{r}}^\dagger t_{\downarrow\boldsymbol{r}-x} - b_{\uparrow\boldsymbol{r}}^\dagger b_{\downarrow\boldsymbol{r}+x} + b_{\uparrow\boldsymbol{r}}^\dagger b_{\downarrow\boldsymbol{r}-x}) \\ & + V(t_{\uparrow\boldsymbol{r}}^\dagger t_{\uparrow\boldsymbol{r}} + t_{\downarrow\boldsymbol{r}}^\dagger t_{\downarrow\boldsymbol{r}} - b_{\uparrow\boldsymbol{r}}^\dagger b_{\uparrow\boldsymbol{r}} - b_{\downarrow\boldsymbol{r}}^\dagger b_{\downarrow\boldsymbol{r}}) + \left(\Delta_N^0 + 2\delta_N^x + 2\delta_N^y\right)(t_{\uparrow\boldsymbol{r}}^\dagger b_{\uparrow\boldsymbol{r}} + t_{\downarrow\boldsymbol{r}}^\dagger b_{\downarrow\boldsymbol{r}}) - \delta_N^x(t_{\uparrow\boldsymbol{r}}^\dagger b_{\uparrow\boldsymbol{r}+x} + t_{\downarrow\boldsymbol{r}}^\dagger b_{\downarrow\boldsymbol{r}+x} + t_{\uparrow\boldsymbol{r}}^\dagger b_{\uparrow\boldsymbol{r}-x} + t_{\downarrow\boldsymbol{r}}^\dagger b_{\downarrow\boldsymbol{r}-x}) \\ & - \delta_N^y(t_{\uparrow\boldsymbol{r}}^\dagger b_{\uparrow\boldsymbol{r}+y} + t_{\downarrow\boldsymbol{r}}^\dagger b_{\downarrow\boldsymbol{r}+y} + t_{\uparrow\boldsymbol{r}}^\dagger b_{\uparrow\boldsymbol{r}-y} + t_{\downarrow\boldsymbol{r}}^\dagger b_{\downarrow\boldsymbol{r}-y}) + \left(\Delta_T^0 + 2\delta_T^x + 2\delta_T^y\right)(t_{\uparrow\boldsymbol{r}}^\dagger b_{\uparrow\boldsymbol{r}+z} + t_{\downarrow\boldsymbol{r}}^\dagger b_{\downarrow\boldsymbol{r}+z}) - \delta_T^x(t_{\uparrow\boldsymbol{r}}^\dagger b_{\uparrow\boldsymbol{r}+x+z} + t_{\downarrow\boldsymbol{r}}^\dagger b_{\downarrow\boldsymbol{r}+x+z} \\ & + t_{\uparrow\boldsymbol{r}}^\dagger b_{\uparrow\boldsymbol{r}-x+z} + t_{\downarrow\boldsymbol{r}}^\dagger b_{\downarrow\boldsymbol{r}-x+z}) - \delta_T^y(t_{\uparrow\boldsymbol{r}}^\dagger b_{\uparrow\boldsymbol{r}+y+z} + t_{\downarrow\boldsymbol{r}}^\dagger b_{\downarrow\boldsymbol{r}+y+z} + t_{\uparrow\boldsymbol{r}}^\dagger b_{\uparrow\boldsymbol{r}-y+z} + t_{\downarrow\boldsymbol{r}}^\dagger b_{\downarrow\boldsymbol{r}-y+z}) \Big] + \text{H.c.}, \end{aligned} \quad \text{(F6)}$$

where $\boldsymbol{r}$ is the unit-cell index and a cubic cell with a lattice constant 1 is assumed.

We obtain surface band spectrum with the real-space lattice periodic Hamiltonian as shown in Fig. 20. First, we focus on the $k_y = 0$ plane. The y direction is removed by fixing k_y, and the surface band spectrum is calculated in a ribbon with a periodic x direction and a finite-z direction. The bulk gap closing occurs at $\Delta_T^0 = 1.1$, which is the point where the Weyl points in 3D BZ touch the $k_y = 0$ plane. This is a topological phase transition point between 2D NI and TI, and when $\Delta_T^0 > 1.1$, we can see topological edge states that connect the valence and conduction band spectra. Next, we focus on the $k_x = 0$ plane. In this case, we consider a ribbon with a periodic y direction and a finite-z direction. Also in this case, a topological phase transition occurs when the Weyl points in 3D BZ touch the $k_x = 0$ plane, $\Delta_T^0 > 1.0$. These results correspond to looking at a particular $\boldsymbol{k}$ slice of the surface state of the 3D WSM. It should be noted that the energies of the surface states are different in the left and right edges in both cases. The emergence of the surface state with edge-dependent energies is consistent with two natural requirements in properties of surface states: (i) edge state should emerge from a gap-closing point of the bulk band spectrum, (ii) a Dirac cone of a time-reversal protected surface state should be located on a TRIM. At the same time, this edge dependence indicates asymmetry of the left and right edges. If the gap closing of the bulk band spectrum occurs on a generic point in the surface BZ, the bulk Hamiltonian is not allowed to have a symmetry that exchanges the left and right edges. Consequently, the position in 2D BZ where a gap-closing point can appear is restricted by crystalline symmetries of the bulk Hamiltonian, which is consistent with Ref. [70].

In conclusion of this Appendix, we have shown the edge dependence of the emergence of the surface states and its relation with symmetries of the bulk Hamiltonian, and demonstrated it with an easy model.

APPENDIX G: TWISTED BHZ MODEL

In this Appendix, we propose a twisted Bernevig-Hughes-Zhang (BHZ) model as a simple model to describe the essential behavior of twisted bilayer $Bi_2(Te_{1-x}Se_x)_3$.

The BHZ model is a well-known effective model of a 2D topological insulator, i.e., a quantum spin Hall insulator. The BHZ model is given with two orbitals and two spin, and the Hamiltonian is typically written as

$$\begin{aligned} & H_{\text{BHZ}}(\boldsymbol{k}) \\ & = (M - Bk^2)\tau_z\sigma_0 + Ak_x\tau_x\sigma_z + Ak_y\tau_y\sigma_0 \\ & = \begin{pmatrix} (M-Bk^2) & Ak^- & & \\ Ak^+ & -(M-Bk^2) & & \\ & & (M-Bk^2) & -Ak^+ \\ & & -Ak^- & -(M-Bk^2) \end{pmatrix}, \end{aligned} \quad \text{(G1)}$$

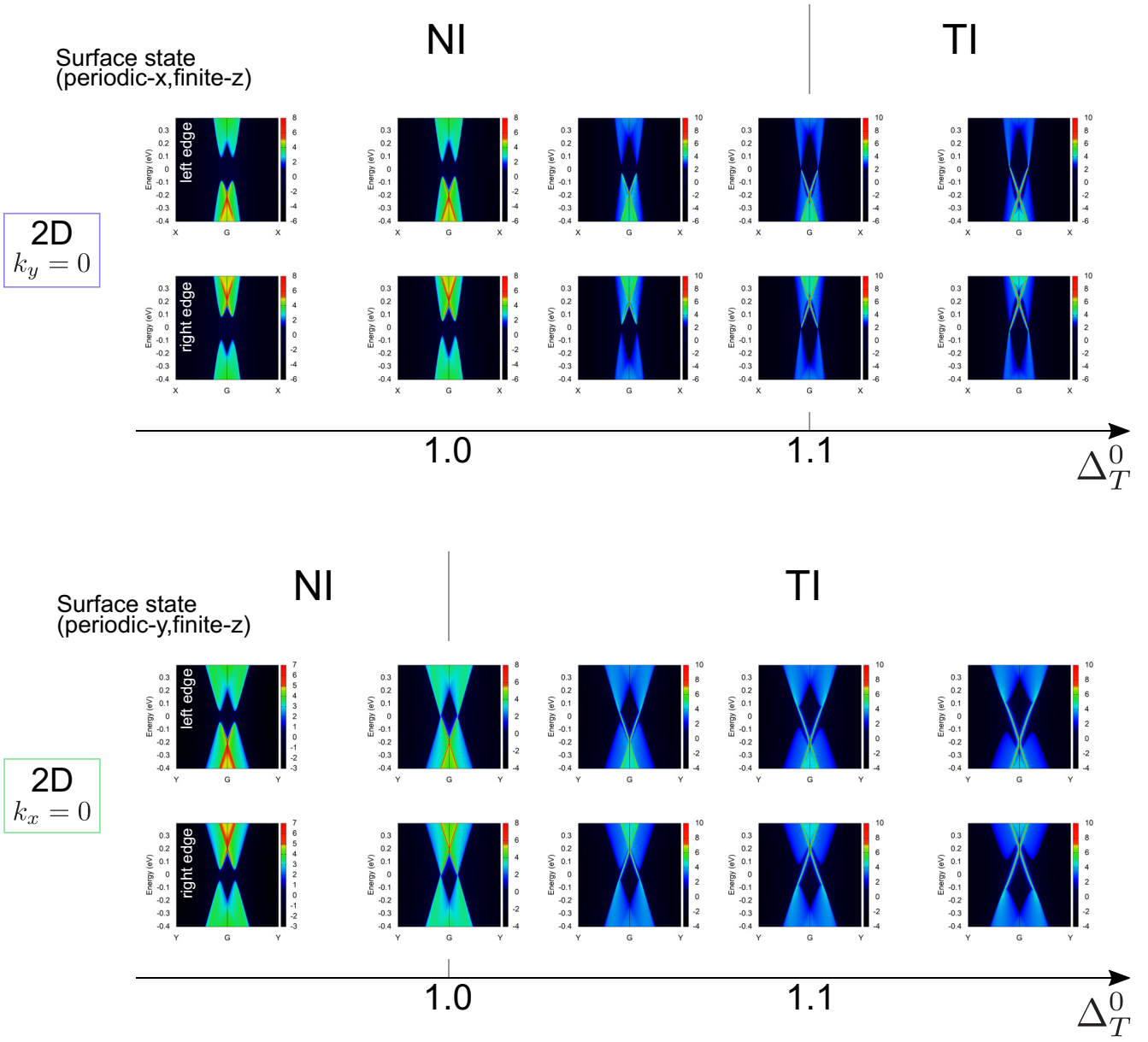

FIG. 20. Phase diagrams of noncentrosymmetric 2D systems and surface band spectra obtained by focusing on the $k_y = 0$ plane (top) and $k_x = 0$ plane (bottom) of the 3D BZ of the WSM (F3). In each phase diagram, the top and bottom density plots are the surface band spectra of the left and right edges, respectively.

where $k^{\pm} = k_x \pm ik_y$, $k^2 = k_x^2 + k_y^2$, and the basis is ordered as $|1,\uparrow\rangle$, $|2,\downarrow\rangle$, $|1,\downarrow\rangle$, $|2,\uparrow\rangle$. This model has the time-reversal symmetry $\mathcal{T}$ and a rotation symmetry around z axis C_θ (perpendicular to the 2D system), and the operators are given as

$$\mathcal{T} = i\sigma_y\mathcal{K}, \quad C_\theta = \begin{pmatrix} e^{i\frac{\theta}{2}} & & & \\ & e^{-i\frac{\theta}{2}} & & \\ & & e^{-i\frac{\theta}{2}} & \\ & & & e^{i\frac{\theta}{2}} \end{pmatrix}. \tag{G2}$$

This model describes a topological insulator when $MB > 0$ and a normal insulator when $BM < 0$.

By introducing a moiré scale oscillation in M, we obtain a twisted BHZ model. To make the model realistic, we transform the basis. We assume that one of the two orbitals is located on the upper layer, and the other on the lower layer, and spin is located on each orbital. This assumption restricts the time-reversal and the rotation operators to be block diagonal with intralayer blocks. We also assume that the moiré oscillating term M should be an interlayer element. To satisfy these assumptions, we transform the Hamiltonian with a unitary matrix

$$\begin{aligned} U &= \frac{1}{2\sqrt{2}}[(\tau_0 + i\tau_y)(\sigma_0 - i\sigma_x) + (\tau_0 - i\tau_y)(\sigma_y + \sigma_z)] \\ &= \frac{1}{\sqrt{2}}\begin{pmatrix} 1 & 0 & -i & 0 \\ 0 & 1 & 0 & -i \\ 0 & -i & 0 & 1 \\ i & 0 & -1 & 0 \end{pmatrix}, \end{aligned} \tag{G3}$$

and obtain a new representation of Hamiltonian

$$\begin{aligned}\tilde{H}_{\mathrm{BHZ}}(\boldsymbol{k}) &= U^{\dagger} H_{\mathrm{BHZ}}(\boldsymbol{k}) U \\ &= (M - Bk^2)\tau_z\sigma_y + Ak_x\tau_x\sigma_0 + Ak_y\tau_y\sigma_0 \\ &= \begin{pmatrix} & Ak^- & & -i(M-Bk^2) \\ Ak^+ & & & \\ i(M-Bk^2) & & & Ak^- \\ & -i(M-Bk^2) & Ak^+ & \end{pmatrix}, \end{aligned} \tag{G4}$$

where the new basis is written as $|1,\uparrow\rangle - i\,|2,\uparrow\rangle$, $|2,\downarrow\rangle + i\,|1,\downarrow\rangle$, $i\,|1,\uparrow\rangle - |2,\uparrow\rangle$, $i\,|2,\downarrow\rangle + |1,\downarrow\rangle$. In this representation, the time-reversal and the rotation operators are written as

$$\tilde{\mathcal{T}} = -\tau_y\sigma_0\mathcal{K}, \quad \tilde{C}_\theta = \begin{pmatrix} e^{i\frac{\theta}{2}} & & & \\ & e^{-i\frac{\theta}{2}} & & \\ & & e^{i\frac{\theta}{2}} & \\ & & & e^{-i\frac{\theta}{2}} \end{pmatrix}. \tag{G5}$$

By assigning $\tilde{H}_{\mathrm{BHZ}}(\boldsymbol{k})$ to $h_{\boldsymbol{r}}^{\alpha\sigma,\beta'\sigma'}(\boldsymbol{k})$ in Eq. (B20), we obtain a Hamiltonian of the twisted BHZ model. By tuning M for three sampling points, we can design a moiré superlattice system with topological and normal insulator domains.

Note that the basis ordering makes a physical difference in a strict sense due to the momentum twisting in Eqs. (B17)–(B19), although it makes no physical difference in an untwisted case. However, the difference is negligible in the small twist angle limit when we consider an effective model around the Γ point in the atomic BZ. We calculate with $\tilde{H}_{\mathrm{BHZ}}(\boldsymbol{k})$, but it is confirmed that almost the same results can be obtained by calculating with $H_{\mathrm{BHZ}}(\boldsymbol{k})$.

Figure 21 shows an example of the twisted BHZ model with $\theta = 0.80°$, $A = 1$, $B = 0.1$, and stacking dependent M that is set to $(M_{AA}, M_{AB}, M_{AC}) = (0.2, -0.3, 0.4)$. Because $MB < 0$ only in the AB-stacking area, the topological insulator domain should appear around the AB-stacking area, as is in twisted bilayer $Bi_2(Te_{1-x}Se_x)_3$. It can be seen that the expected ring-shape edge-state-originated states VB1-3 and their angular momentum ordering are obtained as shown in Figs. 21(b)–21(d). There are also moiré topological bands VB6 and VB7 [Fig. 21(g)], and a corresponding moiré-scale helical edge state is obtained as shown in Fig. 21(h). Because the wave functions of the VB6 [Fig. 21(e)] and VB7 [Fig. 21(f)] are edge-state originated and bulk-state originated, respectively, the obtained moiré-scale helical edge state is an edge state from edge state. These results indicate that the twisted BHZ model is a good simple model that reproduces the properties of twisted bilayer $Bi_2(Te_{1-x}Se_x)_3$. Furthermore, it is also shown that the edge state from edge state is not specific for twisted bilayer $Bi_2(Te_{1-x}Se_x)_3$, but is a general phenomenon in similar moiré systems.

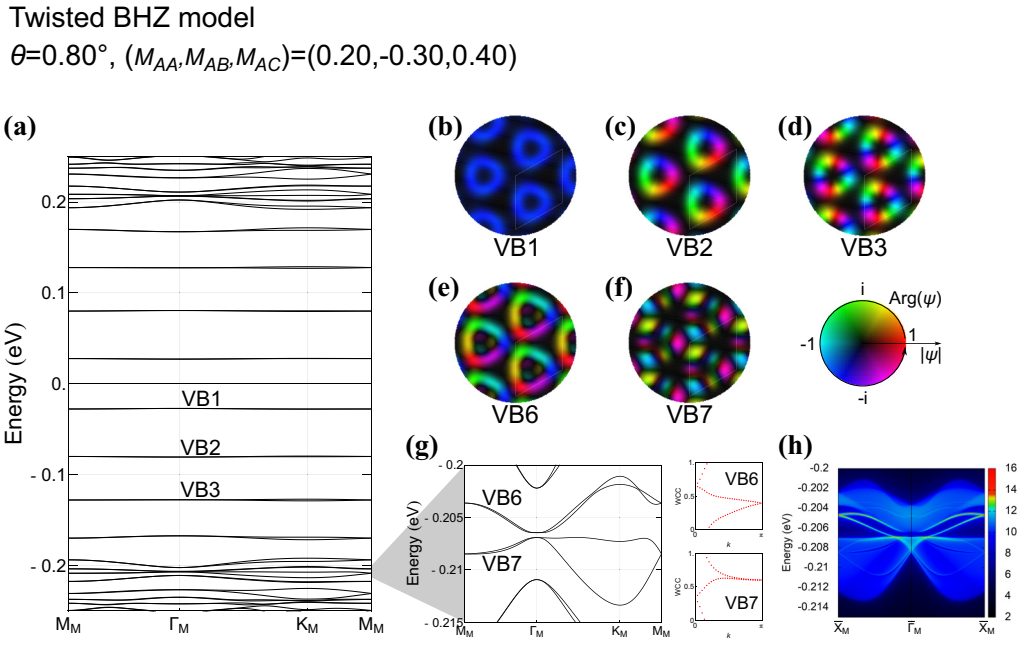

FIG. 21. Example of the twisted BHZ model ($\theta = 0.80°$, $A = 1$, $B = 0.1$). The stacking dependent M is set to $(M_{AA}, M_{AB}, M_{AC}) = (0.2, -0.3, 0.4)$. (a) Moiré band dispersion. (b)–(f) Real-space plot of the wave functions (upper layer, spin up) at the Γ point for VB1, VB2, VB3, VB6, and VB7. (g) Magnified view of the VB6 and VB7 and Wilson loop spectra of them. (h) Moiré edge-state spectrum.

[1] Y. Cao, V. Fatemi, A. Demir, S. Fang, S. L. Tomarken, J. Y. Luo, J. D. Sanchez-Yamagishi, K. Watanabe, T. Taniguchi, E. Kaxiras *et al.*, Correlated insulator behaviour at half-filling in magic-angle graphene superlattices, Nature (London) **556**, 80 (2018).

[2] Y. Cao, V. Fatemi, S. Fang, K. Watanabe, T. Taniguchi, E. Kaxiras, and P. Jarillo-Herrero, Unconventional superconductivity in magic-angle graphene superlattices, Nature (London) **556**, 43 (2018).

[3] H. C. Po, L. Zou, A. Vishwanath, and T. Senthil, Origin of Mott Insulating Behavior and Superconductivity in Twisted Bilayer Graphene, Phys. Rev. X **8**, 031089 (2018).

[4] M. Yankowitz, S. Chen, H. Polshyn, Y. Zhang, K. Watanabe, T. Taniguchi, D. Graf, A. F. Young, and C. R. Dean, Tuning superconductivity in twisted bilayer graphene, Science **363**, 1059 (2019).

[5] A. L. Sharpe, E. J. Fox, A. W. Barnard, J. Finney, K. Watanabe, T. Taniguchi, M. Kastner, and D. Goldhaber-Gordon, Emergent ferromagnetism near three-quarters filling in twisted bilayer graphene, Science **365**, 605 (2019).

[6] Y. Jiang, X. Lai, K. Watanabe, T. Taniguchi, K. Haule, J. Mao, and E. Y. Andrei, Charge order and broken rotational symmetry in magic-angle twisted bilayer graphene, Nature (London) **573**, 91 (2019).

[7] H. Polshyn, M. Yankowitz, S. Chen, Y. Zhang, K. Watanabe, T. Taniguchi, C. R. Dean, and A. F. Young, Large linear-in-temperature resistivity in twisted bilayer graphene, Nat. Phys. **15**, 1011 (2019).

[8] X. Lu, P. Stepanov, W. Yang, M. Xie, M. A. Aamir, I. Das, C. Urgell, K. Watanabe, T. Taniguchi, G. Zhang *et al.*, Superconductors, orbital magnets and correlated states in magic-angle bilayer graphene, Nature (London) **574**, 653 (2019).

[9] A. Kerelsky, L. J. McGilly, D. M. Kennes, L. Xian, M. Yankowitz, S. Chen, K. Watanabe, T. Taniguchi, J. Hone, C. Dean *et al.*, Maximized electron interactions at the magic angle in twisted bilayer graphene, Nature (London) **572**, 95 (2019).

[10] Y. Choi, J. Kemmer, Y. Peng, A. Thomson, H. Arora, R. Polski, Y. Zhang, H. Ren, J. Alicea, G. Refael *et al.*, Electronic correlations in twisted bilayer graphene near the magic angle, Nat. Phys. **15**, 1174 (2019).

[11] Y. Xie, B. Lian, B. Jäck, X. Liu, C.-L. Chiu, K. Watanabe, T. Taniguchi, B. A. Bernevig, and A. Yazdani, Spectroscopic signatures of many-body correlations in magic-angle twisted bilayer graphene, Nature (London) **572**, 101 (2019).

[12] Y. Cao, D. Chowdhury, D. Rodan-Legrain, O. Rubies-Bigorda, K. Watanabe, T. Taniguchi, T. Senthil, and P. Jarillo-Herrero, Strange Metal in Magic-Angle Graphene with near Planckian Dissipation, Phys. Rev. Lett. **124**, 076801 (2020).

[13] M. Serlin, C. Tschirhart, H. Polshyn, Y. Zhang, J. Zhu, K. Watanabe, T. Taniguchi, L. Balents, and A. Young, Intrinsic quantized anomalous Hall effect in a moiré heterostructure, Science **367**, 900 (2020).

[14] P. Stepanov, I. Das, X. Lu, A. Fahimniya, K. Watanabe, T. Taniguchi, F. H. Koppens, J. Lischner, L. Levitov, and D. K. Efetov, Untying the insulating and superconducting orders in magic-angle graphene, Nature (London) **583**, 375 (2020).

[15] Y. Saito, J. Ge, K. Watanabe, T. Taniguchi, and A. F. Young, Independent superconductors and correlated insulators in twisted bilayer graphene, Nat. Phys. **16**, 926 (2020).

[16] B. Hunt, J. D. Sanchez-Yamagishi, A. F. Young, M. Yankowitz, B. J. LeRoy, K. Watanabe, T. Taniguchi, P. Moon, M. Koshino, P. Jarillo-Herrero *et al.*, Massive dirac fermions and hofstadter butterfly in a van der Waals heterostructure, Science **340**, 1427 (2013).

[17] C. R. Dean, L. Wang, P. Maher, C. Forsythe, F. Ghahari, Y. Gao, J. Katoch, M. Ishigami, P. Moon, M. Koshino *et al.*, Hofstadter's butterfly and the fractal quantum Hall effect in moiré superlattices, Nature (London) **497**, 598 (2013).

[18] M. Koshino, N. F. Q. Yuan, T. Koretsune, M. Ochi, K. Kuroki, and L. Fu, Maximally Localized Wannier Orbitals and the Extended Hubbard Model for Twisted Bilayer Graphene, Phys. Rev. X **8**, 031087 (2018).

[19] P. Moon and M. Koshino, Energy spectrum and quantum Hall effect in twisted bilayer graphene, Phys. Rev. B **85**, 195458 (2012).

[20] I. Brihuega, P. Mallet, H. González-Herrero, G. Trambly de Laissardière, M. M. Ugeda, L. Magaud, J. M. Gómez-Rodríguez, F. Ynduráin, and J.-Y. Veuillen, Unraveling the Intrinsic and Robust Nature of van Hove Singularities in Twisted Bilayer Graphene by Scanning Tunneling Microscopy and Theoretical Analysis, Phys. Rev. Lett. **109**, 196802 (2012).

[21] T. Wang, N. F. Q. Yuan, and L. Fu, Moiré Surface States and Enhanced Superconductivity in Topological Insulators, Phys. Rev. X **11**, 021024 (2021).

[22] J. Cano, S. Fang, J. H. Pixley, and J. H. Wilson, Moiré superlattice on the surface of a topological insulator, Phys. Rev. B **103**, 155157 (2021).

[23] S. Carr, S. Fang, and E. Kaxiras, Electronic-structure methods for twisted moiré layers, Nat. Rev. Mater. **5**, 748 (2020).

[24] D. M. Kennes, M. Claassen, L. Xian, A. Georges, A. J. Millis, J. Hone, C. R. Dean, D. Basov, A. N. Pasupathy, and A. Rubio, Moiré heterostructures as a condensed-matter quantum simulator, Nat. Phys. **17**, 155 (2021).

[25] Y. Tang, L. Li, T. Li, Y. Xu, S. Liu, K. Barmak, K. Watanabe, T. Taniguchi, A. H. MacDonald, J. Shan *et al.*, Simulation of Hubbard model physics in WSe_2/WS_2 moiré superlattices, Nature (London) **579**, 353 (2020).

[26] E. C. Regan, D. Wang, C. Jin, M. I. B. Utama, B. Gao, X. Wei, S. Zhao, W. Zhao, Z. Zhang, K. Yumigeta *et al.*, Mott and generalized wigner crystal states in WSe_2/WS_2 moiré superlattices, Nature (London) **579**, 359 (2020).

[27] L. Wang, E.-M. Shih, A. Ghiotto, L. Xian, D. A. Rhodes, C. Tan, M. Claassen, D. M. Kennes, Y. Bai, B. Kim *et al.*, Correlated electronic phases in twisted bilayer transition metal dichalcogenides, Nat. Mater. **19**, 861 (2020).

[28] F. Wu, T. Lovorn, E. Tutuc, I. Martin, and A. H. MacDonald, Topological Insulators in Twisted Transition Metal Dichalcogenide Homobilayers, Phys. Rev. Lett. **122**, 086402 (2019).

[29] Z. Chu, E. C. Regan, X. Ma, D. Wang, Z. Xu, M. I. B. Utama, K. Yumigeta, M. Blei, K. Watanabe, T. Taniguchi, S. Tongay, F. Wang, and K. Lai, Nanoscale Conductivity Imaging of Correlated Electronic States in WSe_2/WS_2 Moiré Superlattices, Phys. Rev. Lett. **125**, 186803 (2020).

[30] Y. Xu, S. Liu, D. A. Rhodes, K. Watanabe, T. Taniguchi, J. Hone, V. Elser, K. F. Mak, and J. Shan, Correlated insulating states at fractional fillings of moiré superlattices, Nature (London) **587**, 214 (2020).

[31] X. Huang, T. Wang, S. Miao, C. Wang, Z. Li, Z. Lian, T. Taniguchi, K. Watanabe, S. Okamoto, D. Xiao *et al.*, Correlated

insulating states at fractional fillings of the WSe_2/WS_2 moiré lattice, Nat. Phys. **17**, 715 (2021).
[32] B. Padhi, R. Chitra, and P. W. Phillips, Generalized wigner crystallization in moiré materials, Phys. Rev. B **103**, 125146 (2021).
[33] Y. Zhang, T. Liu, and L. Fu, Electronic structures, charge transfer, and charge order in twisted transition metal dichalcogenide bilayers, Phys. Rev. B **103**, 155142 (2021).
[34] E. Liu, T. Taniguchi, K. Watanabe, N. M. Gabor, Y.-T. Cui, and C. H. Lui, Excitonic and Valley-Polarization Signatures of Fractional Correlated Electronic Phases in a WSe_2/WS_2 Moiré Superlattice, Phys. Rev. Lett. **127**, 037402 (2021).
[35] F. Wu, T. Lovorn, E. Tutuc, and A. H. MacDonald, Hubbard Model Physics in Transition Metal Dichalcogenide Moiré Bands, Phys. Rev. Lett. **121**, 026402 (2018).
[36] C. Jin, Z. Tao, T. Li, Y. Xu, Y. Tang, J. Zhu, S. Liu, K. Watanabe, T. Taniguchi, J. C. Hone *et al.*, Stripe phases in WSe_2/WS_2 moiré superlattices, Nat. Mater. **20**, 940 (2021)..
[37] X.-J. Zhao, Y. Yang, D.-B. Zhang, and S.-H. Wei, Formation of Bloch Flat Bands in Polar Twisted Bilayers without Magic Angles, Phys. Rev. Lett. **124**, 086401 (2020).
[38] B. Lian, Z. Liu, Y. Zhang, and J. Wang, Flat chern band from twisted bilayer $MnBi_2Te_4$, Phys. Rev. Lett. **124**, 126402 (2020).
[39] H. Zhang, C.-X. Liu, X.-L. Qi, X. Dai, Z. Fang, and S.-C. Zhang, Topological insulators in Bi_2Se_3, Bi_2Te_3 and Sb_2Te_3 with a single Dirac cone on the surface, Nat. Phys. **5**, 438 (2009).
[40] Y. Xia, D. Qian, D. Hsieh, L. Wray, A. Pal, H. Lin, A. Bansil, D. Grauer, Y. S. Hor, R. J. Cava *et al.*, Observation of a large-gap topological-insulator class with a single dirac cone on the surface, Nat. Phys. **5**, 398 (2009).
[41] Y. Chen, J. G. Analytis, J.-H. Chu, Z. Liu, S.-K. Mo, X.-L. Qi, H. Zhang, D. Lu, X. Dai, Z. Fang *et al.*, Experimental realization of a three-dimensional topological insulator, Bi_2Te_3, Science **325**, 178 (2009).
[42] O. V. Yazyev, J. E. Moore, and S. G. Louie, Spin Polarization and Transport of Surface States in the Topological Insulators Bi_2Se_3 and Bi_2Te_3 from First Principles, Phys. Rev. Lett. **105**, 266806 (2010).
[43] C.-X. Liu, H. J. Zhang, B. Yan, X.-L. Qi, T. Frauenheim, X. Dai, Z. Fang, and S.-C. Zhang, Oscillatory crossover from two-dimensional to three-dimensional topological insulators, Phys. Rev. B **81**, 041307(R) (2010).
[44] R. Bistritzer and A. H. MacDonald, Moiré bands in twisted double-layer graphene, Proc. Natl. Acad. Sci. USA **108**, 12233 (2011).
[45] J. Jung, A. Raoux, Z. Qiao, and A. H. MacDonald, Ab initio theory of moiré superlattice bands in layered two-dimensional materials, Phys. Rev. B **89**, 205414 (2014).
[46] K. Momma and F. Izumi, Vesta: A three-dimensional visualization system for electronic and structural analysis, J. Appl. Crystallogr. **41**, 653 (2008).
[47] G. Kresse and J. Furthmüller, Efficient iterative schemes for ab initio total-energy calculations using a plane-wave basis set, Phys. Rev. B **54**, 11169 (1996).
[48] H. Peng, Z.-H. Yang, J. P. Perdew, and J. Sun, Versatile van der Waals Density Functional Based on a Meta-Generalized Gradient Approximation, Phys. Rev. X **6**, 041005 (2016).
[49] A. D. Becke, Density-functional thermochemistry. iii. the role of exact exchange, J. Chem. Phys. **98**, 5648 (1993).
[50] G. Pizzi, V. Vitale, R. Arita, S. Blügel, F. Freimuth, G. Géranton, M. Gibertini, D. Gresch, C. Johnson, T. Koretsune, J. Ibañez-Azpiroz, H. Lee, J.-M. Lihm, D. Marchand, A. Marrazzo, Y. Mokrousov, J. I. Mustafa, Y. Nohara, Y. Nomura, L. Paulatto *et al.*, Wannier90 as a community code: New features and applications, J. Phys.: Condens. Matter **32**, 165902 (2020).
[51] Y. Liu, G. Bian, T. Miller, M. Bissen, and T.-C. Chiang, Topological limit of ultrathin quasi-free-standing Bi_2Te_3 films grown on si(111), Phys. Rev. B **85**, 195442 (2012).
[52] Y. Zhang, K. He, C.-Z. Chang, C.-L. Song, L.-L. Wang, X. Chen, J.-F. Jia, Z. Fang, X. Dai, W.-Y. Shan, S.-Q. Shen, Q. Niu, X.-L. Qi, S.-C. Zhang, X.-C. Ma, and Q.-K. Xue, Crossover of the three-dimensional topological insulator Bi_2Se_3 to the two-dimensional limit, Nat. Phys. **6**, 584 (2010).
[53] T. Förster, P. Krüger, and M. Rohlfing, *GW* calculations for Bi_2Te_3 and Sb_2Te_3 thin films: Electronic and topological properties, Phys. Rev. B **93**, 205442 (2016).
[54] Q. Wu, S. Zhang, H.-F. Song, M. Troyer, and A. A. Soluyanov, Wanniertools: An open-source software package for novel topological materials, Comput. Phys. Commun. **224**, 405 (2018).
[55] S. Murakami, S. Iso, Y. Avishai, M. Onoda, and N. Nagaosa, Tuning phase transition between quantum spin Hall and ordinary insulating phases, Phys. Rev. B **76**, 205304 (2007).
[56] S. Murakami, Phase transition between the quantum spin Hall and insulator phases in 3d: emergence of a topological gapless phase, New J. Phys. **9**, 356 (2007).
[57] J. Chalker and P. Coddington, Percolation, quantum tunnelling and the integer Hall effect, J. Phys. C: Solid State Phys. **21**, 2665 (1988).
[58] H. Obuse, A. Furusaki, S. Ryu, and C. Mudry, Two-dimensional spin-filtered chiral network model for the $\mathbb{Z}_2$ quantum spin-Hall effect, Phys. Rev. B **76**, 075301 (2007).
[59] H. Obuse, A. Furusaki, S. Ryu, and C. Mudry, Boundary criticality at the anderson transition between a metal and a quantum spin Hall insulator in two dimensions, Phys. Rev. B **78**, 115301 (2008).
[60] H. Obuse, S. Ryu, A. Furusaki, and C. Mudry, Spin-directed network model for the surface states of weak three-dimensional $\mathbb{Z}_2$ topological insulators, Phys. Rev. B **89**, 155315 (2014).
[61] S. Ryu, C. Mudry, H. Obuse, and A. Furusaki, The network model for the quantum spin Hall effect: two-dimensional dirac fermions, topological quantum numbers and corner multifractality, New J. Phys. **12**, 065005 (2010).
[62] J. D. Sanchez-Yamagishi, J. Y. Luo, A. F. Young, B. M. Hunt, K. Watanabe, T. Taniguchi, R. C. Ashoori, and P. Jarillo-Herrero, Helical edge states and fractional quantum Hall effect in a graphene electron–hole bilayer, Nat. Nanotechnol. **12**, 118 (2017).
[63] Q. Tong, H. Yu, Q. Zhu, Y. Wang, X. Xu, and W. Yao, Topological mosaics in moiré superlattices of van der Waals heterobilayers, Nat. Phys. **13**, 356 (2017).
[64] P. Rickhaus, J. Wallbank, S. Slizovskiy, R. Pisoni, H. Overweg, Y. Lee, M. Eich, M.-H. Liu, K. Watanabe, T. Taniguchi *et al.*, Transport through a network of topological channels in twisted bilayer graphene, Nano Lett. **18**, 6725 (2018).
[65] P. San-Jose and E. Prada, Helical networks in twisted bilayer graphene under interlayer bias, Phys. Rev. B **88**, 121408(R) (2013).

[66] D. K. Efimkin and A. H. MacDonald, Helical network model for twisted bilayer graphene, Phys. Rev. B **98**, 035404 (2018).

[67] S. Huang, K. Kim, D. K. Efimkin, T. Lovorn, T. Taniguchi, K. Watanabe, A. H. MacDonald, E. Tutuc, and B. J. LeRoy, Topologically Protected Helical States in Minimally Twisted Bilayer Graphene, Phys. Rev. Lett. **121**, 037702 (2018).

[68] A. Ramires and J. L. Lado, Electrically Tunable Gauge Fields in Tiny-Angle Twisted Bilayer Graphene, Phys. Rev. Lett. **121**, 146801 (2018).

[69] T. Kariyado and A. Vishwanath, Flat band in twisted bilayer bravais lattices, Phys. Rev. Res. **1**, 033076 (2019).

[70] J. Yu and C.-X. Liu, Piezoelectricity and topological quantum phase transitions in two-dimensional spin-orbit coupled crystals with time-reversal symmetry, Nat. Commun. **11**, 2290 (2020).

[71] A. A. Burkov and L. Balents, Weyl Semimetal in a Topological Insulator Multilayer, Phys. Rev. Lett. **107**, 127205 (2011).

[72] G. B. Halász and L. Balents, Time-reversal invariant realization of the weyl semimetal phase, Phys. Rev. B **85**, 035103 (2012).